# Base metal sulphide geochemistry of southern African mantle eclogites (Roberts Victor): Implications for cratonic mafic magmatism and metallogenesis

**Hannah S.R Hughes[1,8*], Charlie Compton-Jones[1], Iain McDonald[2], Ekaterina S. Kiseeva[3,4], Vadim S. Kamenetsky[5,6], Gavyn Rollinson[1], Judith A. Coggon[7], Judith A. Kinnaird[1,8], Grant M. Bybee[8]**

[1]Camborne School of Mines, University of Exeter, Cornwall Campus, Penryn, Cornwall, TR10 9FE, UK
[2]School of Earth and Ocean Sciences, Cardiff University, Main Building, Cardiff CF10 3AT, UK
[3]Department of Earth Sciences, University of Oxford, Oxford, OX1 3AN, UK
[4]School of Biological, Earth and Environmental Sciences, University College Cork, Cork, Ireland
[5]ARC Centre of Excellence in Ore Deposits and School of Earth Sciences, University of Tasmania, Hobart, TAS 7001, Australia
[6]Institute of Experimental Mineralogy, Chernogolovka, Russia
[7]School of Ocean and Earth Science, University of Southampton, Waterfront Campus, European Way, Southampton SO14 3ZH, UK
[8]School of Geoscience, University of the Witwatersrand, Johannesburg, South Africa

*Corresponding author email: h.hughes@exeter.ac.uk

*Submission to:* ***Lithos*** [1]

Keywords**:** Eclogite, base metal sulphide, PGE, Kaapvaal, Roberts Victor, metallogenesis

[1] **Abbreviations**: base metal sulphide (BMS), platinum-group elements (PGE), electron probe microanalysis (EPMA), scanning electron microscope (SEM), laser ablation inductively coupled plasma mass spectrometry (LA-ICP-MS), working distance (WD), back scattered electron (BSE), energy dispersive spectrometer (EDS)

**Abstract**

Platinum-group elements (PGE) display a chalcophile behaviour and are largely hosted by base metal sulphide (BMS) minerals in the mantle. During partial melting of the mantle, BMS release their metal budget into the magma generated. The fertility of magma sources is a key component of the mineralisation potential of large igneous provinces (LIP) and the origin of orthomagmatic sulphide deposits hosted in cratonic mafic magmatic systems. Fertility of mantle-derived magma is therefore predicated on our understanding of the abundance of metals, such as the PGE, in the asthenospheric and lithospheric mantle. Estimations of the abundance of chalcophile elements in the upper mantle are based on observations from mantle xenoliths and BMS inclusions in diamonds. Whilst previous assessments exist for the BMS composition and chalcophile element budget of peridotitic mantle, relatively few analyses have been published for eclogitic mantle. Here, we present sulphide petrography and an extensive *in situ* dataset of BMS trace element compositions from Roberts Victor eclogite xenoliths (Kaapvaal Craton, South Africa). The BMS are dominated by pyrite-chalcopyrite-pentlandite (± pyrrhotite) assemblages with S/Se ratios ranging 1200 to 36,840 (with 87% of analyses having S/Se < 10,000). Total PGE abundance in BMS range from 0.17 to 223 ppm. We recognise four end-member compositions (*types i to iv*), distinguished by total PGE abundance and Pt/Pd and Au/Pd ratios. The majority of BMS have low PGE abundances (< 10 ppm) but *Type iv* BMS have the highest concentration of PGE recorded in eclogites so far (> 100 ppm) and are characteristically enriched in Os, Ir, Ru and Rh. Nano- and micron-scale Pd-Pt antimonide, telluride and arsenide platinum-group minerals (PGM) are observed spatially associated with BMS. We suggest that the predominance of pyrite in the xenoliths reflects the process of eclogitisation and that the trace element composition of the eclogite BMS was inherited from oceanic crustal protoliths of the eclogites, introduced into the SCLM via ancient subduction during formation of the Colesberg Magnetic Lineament c. 2.9 Ga and the cratonisation of the Kaapvaal Craton. Crucially, we demonstrate that the PGE budget of eclogitic SCLM may be substantially higher than previously reported, akin to peridotitic compositions, with significant implications for the PGE fertility of cratonic mafic magmatism and metallogenesis. We quantitatively

assess these implications by modelling the chalcophile geochemistry of an eclogitic melt component in parental magmas of the mafic Rustenburg Layered Suite of the Bushveld Complex.

## 1. Introduction

Platinum-group elements (PGE; Os, Ir, Ru, Rh, Pt, Pd) and most transition metals have an affinity for sulphur (i.e., are chalcophile) and are largely hosted by base metal sulphide (BMS) minerals in the mantle (e.g., Barnes et al., 2015; Lorand & Luguet, 2016; Luguet & Reisberg, 2016 and references therein). During partial melting of the mantle, BMS undergo melting and release their metal budget into the magma generated. Hence if a mantle source region has BMS strongly enriched in PGE or other metals, magma produced by partial melting of that region (particularly a significant degree of partial melting, e.g., > 20%) will also be enriched in these elements and thus will be 'fertile'. However, there are differences in the compatibility and thus mobility of individual PGE and their host minerals, adding complexity to the partial melting regime and correspondingly the concentration of these metals in magma generated. For example, Ir-group PGE (IPGE; Os, Ir and Ru, which behave comparably to Ni and Co) can be hosted by sulphide as well as discrete platinum-group minerals (PGM), spinel-group minerals (e.g., chromite) and even olivine (e.g., Brenan & Andrews, 2001; Ahmed & Arai, 2002; Pitcher et al., 2009; Locmellis et al., 2013). In contrast, most Pt-group PGE (PPGE; Rh, Pt, Pd which broadly behave in a similar geochemical manner to Cu and Au) are largely hosted by sulphides only, although Pt may also be hosted by discrete PGM, either within or on the margins of BMS or sometimes as alloys with other PGE (notably IPGE) (e.g., Lorand et al., 2013; Lorand and Luguet, 2016 and references therein; Gonzalez-Jimenez et al., 2020). Thus the PGE have been subdivided based to their behaviour during partial melting of the mantle and apparent compatibility within silicate and oxide minerals, such that IPGE are 'compatible' and PPGE are 'incompatible'. Further, at the pressures and temperatures at which most mantle partial melting takes place, the sulphide budget of the mantle may occur as two coexisting phases: an Fe-rich monosulphide solid solution (MSS) typically relatively enriched in IPGE, and a comparatively PPGE-enriched Ni-Cu sulphide (e.g., Alard et al., 2000; Bockrath et al., 2004; Lorand et al., 2013 and references therein). Combined, the fertility of a mantle source is a concept fundamental to global 'metallogenesis' (the regional-to-global distribution of metals linked by magmatic and tectonic processes) and likely has further implications for the metallic signature, or

80 'metal basket', of mineralisation linked to mantle-derived (ultra)mafic magmatic systems (e.g., Hughes
81 et al., 2015, 2017).

82 Estimations of the abundance of chalcophile elements in the cratonic subcontinental lithospheric
83 mantle (SCLM, and various regions and lithologies thereof) are based on observations from mantle
84 xenoliths and diamond inclusions (e.g., Bulanova et al., 1996; McDonald et al., 1996; Becker et al.,
85 2006; Aulbach et al., 2012; McDonald et al., 2017). Indeed, mantle xenoliths containing BMS minerals
86 and sulphide inclusions within diamonds provide our only direct insight into the abundance of
87 chalcophile elements at depth. BMS contained within these SCLM-derived samples (whether in
88 xenoliths or as inclusions in diamonds) are commonly divided into two, E-type (eclogitic) and P-type
89 (peridotitic) based on the sulphide composition and associated silicate phase assemblage (e.g., Stachel
90 & Harris, 2008; Kiseeva et al., 2017a). For example, published trace element data from BMS inclusions
91 in diamonds and mantle xenoliths suggest a significant difference in the concentration of chalcophile
92 elements including PGE and other precious and transition metals, between eclogitic and peridotitic
93 mantle (e.g., McDonald et al., 2017).

94 Globally, most published mantle xenolith *in situ* BMS analyses and diamond BMS inclusion data report
95 major element and Re-Os isotopic compositions, and lack information regarding the concentration of
96 PGE and other minor or trace metals (with the notable exceptions of Aulbach et al. (2012) for BMS
97 inclusions in E-type diamonds, and Gréau et al. (2008) and Burness et al. (2020) for cratonic eclogite
98 xenoliths). Other published PGE data for eclogites are bulk rock analyses – such as McDonald & Viljoen
99 (2006) for Orapa eclogite xenoliths and Dale et al. (2009) for ophiolitic eclogites. Eclogite xenolith data
100 from Gréau et al. (2008) and Burness et al. (2020) indicate that the PGE and precious metal budget for
101 this mantle lithology is very low; this is corroborated by the composition of E-type diamond BMS
102 inclusions (e.g., Orapa, Botswana, McDonald et al., 2017; Diavik, Canada, Aulbach et al., 2012) in
103 comparison to the relatively PGE-rich composition of P-type diamond BMS inclusions (Bulanova et al.,
104 1996). In this contribution we present *in situ* analyses of BMS in eclogite xenoliths from the Roberts

Victor kimberlite in South Africa and use these data to estimate the precious metal and metalloid budget of the eclogitic SCLM of the Kaapvaal Craton. We examine the range of the eclogitic sulphide-hosted metal budget using the abundant BMS in the Roberts Victor xenoliths and compare these to different mantle source lithologies (e.g., peridotitic) to explore the implications of mantle source characteristics for the fertility of mantle-derived magmas, mineralisation linked to (ultra)mafic magmatic systems and metallogenesis.

### *1.1 Geological setting*

The Kaapvaal Craton of southern African is one of the oldest and thickest sections of crust on Earth (Erikkson et al., 2011). After stabilising c. 3.2-2.8 Ga, it collided with the Zimbabwe Craton becoming sutured by the Limpopo Belt and thus forming the Kalahari Craton (e.g., de Wit et al., 1992; Schmitz et al., 2004; Simon et al., 2007; Brey and Shu, 2018). Largely composed of tonalite-trondhjemite-granodiorite (TTG) suites and Archaean granitic gneisses, the Kaapvaal Craton comprises four crustal blocks: the Kimberley Block (Western Block), the Witwatersrand and Swaziland blocks (Eastern Block), and the Pietersburg Block (e.g., Good and de Wit 1997; Griffin et al., 2003a and references therein) – Figure 1.

The Witwatersrand and Kimberley blocks are separated by the Colesberg magnetic lineament, which marks a palaeo-subduction zone between the two blocks that collided c. 2.88 Ga (Schmitz et al., 2004; Brey and Shu, 2018 and references therein) resulting in subduction of c. 2.95 Ga oceanic lithosphere underneath the Western Block (Shu et al., 2013). This process corresponds with a c. 2.9 Ga major metasomatic event in the Kaapvaal Craton, which led to eclogite and eclogite-hosted diamond formation (e.g., Jacob et al., 2003; Richardson et al., 2004) recorded in samples from the Roberts Victor, Jagersfontein, Kimberley and Jwaneng kimberlites. These events also coincide with a peak in Re-Os ages of the Kimberley Block (Schmitz et al., 2004 and references therein) and S-isotopic mass-independent fractionation (S-MIF) is evidence for surficial sulphur having been transferred to the SCLM by this time (e.g., Thomassot et al., 2017).

The Kaapvaal Craton has experienced several episodes of kimberlitic intrusions since at least 1.2 Ga, and notably over the last c. 200 Myr, coincident with the break-up of Gondwana ca. 180 Ma (Jelsma et al., 2009). A number of kimberlites, including the 125 Ma Roberts Victor kimberlite pipe, occur on, or proximal to, the Colesberg magnetic lineament (e.g., Schmitz et al., 2004 and Fig. 1). Roberts Victor lies about 40 km east of Boshof on the Kaapvaal Craton (Field et al., 2008). It consists of at least seven different kimberlites, among which are two pipes and two dykes (Gurney and Kirkley, 1996; Field et al., 2008). The kimberlites belong to the micaceous Group II kimberlites and the phlogopite/biotite ages range from 124 to 128 Ma (e.g., Tappe et al., 2018).

### *1.2 Roberts Victor eclogite xenoliths*

For more than 50 years, the eclogite xenoliths of Roberts Victor kimberlite have been extensively studied (e.g., MacGregor and Carter, 1970; Garlick et al., 1971; Manton and Tatsumoto, 1971; Harte and Gurney, 1975; Ozima and Saito, 1975; Hatton and Gurney, 1977; Kramers, 1979; MacGregor and Manton, 1986; Ongley et al., 1987; Sautter and Harte, 1988; Viljoen et al., 1991; Jacob et al., 2003, 2005; Huang et al., 2010; Gréau et al., 2013; Kiseeva et al., 2017b; Burness et al., 2020). Early studies recognised that an unusual feature of this pipe is its substantially larger proportion of mafic xenoliths in comparison to ultramafic (~80:20) (Chen, 1971; Macgregor and Carter, 1970), and eclogite xenoliths are up to 80 cm in diameter (Gurney and Kirkley, 1996). Isotopic studies of the eclogite xenoliths led researchers to suggest that their protolith was altered oceanic crust (Ongley et al., 1987), subsequently confirmed by petrological and geochemical studies (e.g. Jacob, 2004).

Based on the textural characteristics and major and minor element composition of garnet and clinopyroxene, Macgregor and Carter (1970) identified two types of eclogitic xenoliths in Roberts Victor kimberlites: Texturally, Type I is more altered than Type II, and contains secondary material surrounding every primary grain of garnet or clinopyroxene. This secondary material in Type I xenoliths

154 is compositionally distinguished by high $Na_2O$ ( $\geq$ 0.07 wt.%) in garnet and high $K_2O$ ( $\geq$ 0.08 wt.%) in
155 clinopyroxene. In Type II eclogites, garnet and clinopyroxene contain $\leq$ 0.07 wt.% $Na_2O$ and $\leq$ 0.08
156 wt.% $K_2O$, respectively. Huang et al. (2012) and Gréau et al. (2011) reported that eclogite xenoliths of
157 both types were sourced from similar depths (170-200 km, using the garnet-clinopyroxene
158 geothermometer of Krogh (1988) and pressure estimates derived from projections of the geotherm),
159 close to the base of the Kaapvaal SCLM. Huang et al. (2012) also expanded their classification,
160 identifying higher concentrations of light rare earth elements (LREE) and large ion lithophile elements
161 (LILE) in Type I xenoliths.

162 Mantle 'metasomatism' evidenced by Roberts Victor eclogites has been investigated: Huang et al.
163 (2014) reported zones of alteration observed within one xenolith and proposed that these may reflect
164 multiple pulses of metasomatism that resulted from interaction in an open system with mantle fluids
165 of varying major and trace element and isotopic compositions. Kiseeva et al. (2017b) investigated a
166 Type I eclogite xenolith and, similarly to the previous studies, reported enrichments in Na, K, Ba, Ti
167 and REE. However, the authors hypothesised that the origin of this metasomatic alteration could be
168 in the incipient melting of the eclogite itself rather than introduction of mantle metasomatic fluids or
169 melts. We ask, what effect would metamorphism, incipient melting, or open system metasomatism
170 have on the BMS composition and chalcophile element budget of these eclogites, and can we
171 distinguish between these processes?

172

173 **2. Methodology and analytical techniques**

174 ***2.1 Samples and petrography***

175 Seven individual diamond-free Roberts Victor eclogite xenoliths, mostly ranging in size from 3 to 5 cm,
176 were used in this study. Detailed silicate textural and chemical analyses are available for the largest of
177 these samples (*SS2*, sized 20 x 15 x 7 cm) (Kiseeva et al., 2017b). All samples were chosen as

representative samples from this pipe and are bimineralic with omphacitic clinopyroxene and pyrope-almandine garnet as the modal minerals and interpreted as primary phases.

Petrographic observations were made using reflected and transmitted light microscopy. Photomicrographs of samples except SS2 were captured using a Nikon Eclipse E600 Pol microscope with a 5MP Nikon Digital Sight camera at the Camborne School of Mines (CSM, University of Exeter). Further petrographic examination was carried out using back-scattered electron (BSE) imaging on a JEOL JXA-8200 Superprobe electron probe microanalyser (EPMA, located at CSM) as a scanning electron microscope (SEM) using X-ray Energy Dispersive Spectrometers (EDS) and under high vacuum at $7 \times 10^{-4}$ Pa. For BSE imaging, the instrument was run with an accelerating voltage of 15 kV or 20 kV with a 1 nA beam current. Searches for platinum-group minerals (PGM) were conducted by energy dispersive x-ray spectrometry (EDS) on a Schottky field emission Hitachi SU-70 field emission SEM at the CSL (Central Science laboratory), University of Tasmania, which is equipped with an Oxford AZTec microanalysis system with X-Max80 SDD EDS detector. Operating conditions were accelerating voltage 15 kV, probe current 300–400 pA, and spot size 100–200 nm. BSE imaging of the sample SS2 was conducted using CAMECA SX-5 FE at the University of Oxford. Table 1 provides sample information regarding the texture and location of BMS in the seven eclogite xenoliths.

### *2.2 QEMSCAN*

The mineral assemblage of three polished thin sections (RV-IM-01, RV-IM-15 and RV-IM-18) was analysed using a QEMSCAN® 4300 at CSM, University of Exeter, UK (Gottlieb et al., 2000, Goodall et al., 2005, Goodall and Scales 2007). The software packages iMeasure version 4.2SR1 and iDiscover 4.2SR1 and 4.3 (Rollinson et al. 2011) were used for sample measurement and data processing. The samples were carbon coated to 25 nm prior to analysis using an Emitech K950 carbon coater.

The QEMSCAN® 4300 system settings were the default of 25 kV, 5 nA, a 1000 X-ray count rate per pixel, a WD of around 22 mm under high vacuum and beam calibration every 30 minutes. The

fieldscan measurement mode was used to analyse the samples. For sample RV-IM-01 the whole sample area (18 x 27mm approximately) was measured at an X-ray resolution/pixel spacing of 10 microns and a 1500 micron squared field size (x 43 magnification), with two smaller areas scanned at an X-ray resolution/pixel spacing of 1 microns and a 300 micron squared field size (x 224 magnification) for improved detail. The two smaller areas had scan areas of 1 $mm^2$ and 2 $mm^2$ approximately.

For samples RV-IM-15 and RV-IM-18, the fieldscan measurement mode was used to analyse selected small areas at an X-ray resolution/pixel spacing of 1 micron and a 300 micron squared field size (x 238 magnification) for improved detail. For sample RV-IM-15 three small areas were measured on the thin section with scan areas of ~1$mm^2$, ~2 $mm^2$ and ~3 $mm^2$. For sample RV-IM-18, two small areas were measured on the thin section, both with scan areas of 1 $mm^2$ approximately. The areas were selected to target sulphides and provide high resolution data.

Data processing and database development was employed to add and improve SIP (database) categories to match the samples and all of the mineral categories were checked (examination of elemental abundance, elemental ratios, BSE). Specific attention was given to the sulphide minerals such as pyrite, pyrrhotite, chalcopyrite, pentlandite/violarite and sphalerite. The effects of excitation volume were also checked and boundary effect database entries added to handle these. Finally, boundary phase processors were applied to improve edge effects and remove rogue pixels. Data collection and processing followed in-house QC/QA procedures. A summary of QEMSCAN BMS mineral association data are presented in Table 2 and a full list of all mineral association data are available in Supplementary Table A.

### *2.3 BMS Mineral chemistry*

#### *2.3.1 Electron Probe Microanalysis (EPMA)*

Samples were coated with ~25 nm of carbon. Quantitative spot microanalyses of BMS per xenolith were obtained using a JEOL JXA-8200 Superprobe at CSM. Both instruments were each fitted with four

WDS detectors, each of which were fitted with two crystals (TAP, LDE, LIF or PET). Analyses at CSM were carried out at a 15 keV accelerating voltage, 14 nA beam current and 10 µm spot size. Counting times for all elements were 20 s for the peak and 10 s for the background. Major elements analysed for sulphides are S, Fe, Ni, Cu and Co. Elements were calibrated prior to analysis with MicroAnalysis Consultants Ltd and Astimex Standards Ltd mineral standards including Astimex pyrite, pentlandite, and metallic standards for Co and Cu. Accuracy was assessed by measuring multiple spot analyses of selected sulphide mineral standards (Astimex pyrite and pentlandite) – see Supplementary Table B. Lower limits of detection (LLD) were calculated using 3σ and are ≤0.12 wt.% for S, ≤0.15 wt.% for Fe, ≤0.17 wt.% for Cu, 0.07 wt.% for Co and 0.14 wt.% for Ni respectively. A summary of EPMA sulphide data are presented in Table 3 and a full list of data are available in Supplementary Table C.

*2.3.2 Laser ablation inductively coupled plasma mass spectrometry (LA-ICP-MS)*

Time-resolved analysis (TRA) by LA-ICP-MS was performed on each BMS analysed at Cardiff University in two time periods using a UP213 Laser Ablation system coupled initially to a Thermo X Series 2 ICP-MS (RV-IM samples) and later to a Thermo iCAP RQ ICP-MS (SS2 samples). Line analyses were used and all lines were independently calibrated. Where size permitted, sulphides underwent multiple line analyses. A minimum length of ~80 µm and a beam diameter of 40 µm were used, with laser operating conditions of 10 Hz frequency, 0.063 mJ at ~ 5 $Jcm^{-2}$ and sample translation at 6 µm $sec^{-1}$. Acquisition times ranged from 50 to 200 seconds with a gas blank measured for 20 seconds prior to laser ablation. Major element abundances (Fe, Ni, Cu, S) of the sulphide were measured by EPMA (section 2.3.1) and a representative $^{33}S$ per BMS was used as an internal standard for trace element calibration. This was typically 45 wt.% S as a mean of pentlandite, chalcopyrite, rare pyrrhotite, and pyrite, and in line with the mean S concentration of sulphides in eclogitised gabbros (47.5 wt.%) in the Zermatt-Saas ophiolite (Dale et al., 2009). Gas blank subtraction, TRA timeslice selection and internal standard corrections were carried out on Thermo Plasmalab software (RV-IM samples) and Qtegra software (SS2 samples).

Five synthetic Ni-Fe-S quenched sulphide standards (numbered 1 to 5) were used for calibration. These included S, Ni, Fe and Cu as major elements and Co, As, Se, Ru, Rh, Pd, Ag, Cd, Sb, Te, Re, Os, Ir, Pt, Au and Bi as trace elements (and on some analytical runs, Mo and Pb). See Prichard et al. (2013) for the compositions and details of analytical methods for these standards and Smith et al. (2014) for further procedural details. Standards 1 to 3 were used for calibration of Fe, Ni, Cu, Co, Zn and Cd and matrix-matched corrections for argide species that interfere with light PGE isotopes ($^{59}Co^{40}Ar$, $^{61}Ni^{40}Ar$, $^{63}Cu^{40}Ar$, $^{65}Cu^{40}Ar$ and $^{66}Zn^{40}Ar$). Standard 1 (bearing 143 ppm Cd) was also used in corrections for $^{106}Cd$ on $^{106}Pd$ and $^{108}Cd$ on $^{108}Pd$. Independent corrections for isotopes of the same element (e.g., $^{66}Zn^{40}Ar$ and $^{106}Cd$ on $^{106}Pd$, and $^{108}Cd$ on $^{108}Pd$) showed < 20% variance for Ru isotopes at concentrations from 0.1-0.2 ppm Ru and 3-10% for Pd isotopes at concentrations around 1 ppm Pd, indicating that the correction criteria are appropriate.

Accuracy for PGE and Au was monitored by analysis of the Laflamme-Po724T ('Mem FeS') pyrrhotite standard and the University of Quebec at Chicoutimi (UQAC) FeS1 sulphide standard, as unknowns against the Cardiff quenched sulphide standards (results in Supplementary Table D). Based on these two standards, 1σ precision is typically from 1.6 to 11.2%. A summary of LA-ICP-MS data are presented in Table 4 and a full list of data are available in Supplementary Table E, including argide and isobaric-corrected data with values displayed by isotope (for Ru, Rh and Pd).

## 3. Results

### *3.1 Sample petrography – QEMSCAN® and microscopy*

QEMSCAN® was used to assess the intricate mineralogical and textural relationships within the xenoliths and particularly the BMS. Figure 2a presents a full thin section false colour mineral map of sample RV-IM-01 with higher resolution scans of two BMS in Figures 2b-e. Pyrope and omphacite form up to ~90% of the modal mineralogy (Table 1). These larger 'primary' grains are typically fringed by channels of finer, intergrown (locally spongy) 'secondary' accessory minerals including Na-poor

diopsidic clinopyroxene, albite, K-feldspar, and biotite, with very minor alteration to chlorite and talc (Figure 2 and Supplementary Figure B). Ilmenite and rutile occur as < 1 mm rare accessory grains in some samples.

Through a combination of reflected light microscopy, SEM mapping and QEMSCAN® analyses, BMS are found to be dominated by pyrite (Fig. 3c-f, Table 2), with lesser pentlandite, Ni-rich pyrite and chalcopyrite, and rare pyrrhotite (e.g., Fig. 2b-c, 3a-b, Table 2). Pyrite typically bears fine lamallae or net-textured pentlandite, or a Ni-rich pyrite (possibly vaesite and/or violarite or millerite) and rimmed by blocky chalcopyrite. Pentlandite and/or Ni-rich pyrite typically form < 5 to ~45 area % based on visual estimates and confirmed by QEMSCAN® quantitative data for a representative selection of BMS scanned (Table 2). Chalcopyrite is visible in the majority of BMS but is generally a minor phase in most BMS (< 15%, e.g., Table 2) although BMS lacking a significant Fe-sulphide component and only containing pentlandite and chalcopyrite were identified (e.g., Supplementary Figure B(b)). These specimens have a higher apparent chalcopyrite abundance (up to 42 %). However, we note that the *apparent* proportions of end-member sulphide minerals within the BMS grains are dependent upon the level of exposure achieved through polished thin section or polished block production. These are likely to vary significantly depending on whether the exposed 2D surface cross-cuts the centre of a BMS, or it's margin.

The BMS grains occur in two principal textural settings: (i) predominantly interstitial to the primary silicate minerals along grain boundaries of pyrope and omphacite (e.g., Supplementary Fig. B(d)) and in the channels of finer 'secondary' minerals (e.g., Fig. 2b-c and Supplementary B a-b) and (ii) as inclusions and/or embayments within both these silicates (e.g., Fig. 2d-e and Supplementary Fig. B c and e). Included BMS range in diameter from approximately 70 to 150 µm. They are either rounded or have a polygonal shape. The embayments are locally accompanied by a rim of fine spongy 'secondary' clinopyroxene with variable Na content. In contrast, BMS grains interstitial to the 'primary' silicate mineralogy of the xenoliths occur as rounded droplets (Fig. 3a-b) or as highly irregular shapes

(Fig. 3c-f) and typically range from 50 to > 500 µm in width, with most > 200 µm. Most interstitial BMS, and some embayments, preserve thin stringers of pyrite intermingled in the channels with 'secondary' silicates, especially clinopyroxene (e.g., Fig. 2d-e, 3e-f). Overall, 79% of BMS observed in this study are interstitial and 21% are included or embayed (Table 5). We observed no systematic difference in the proportion of end-member sulphide minerals (e.g., chalcopyrite, pentlandite, pyrite or pyrrhotite) according to BMS position within the xenolith (included, embayment, or interstitial).

### *3.2 BMS major element geochemistry (by EPMA)*

A summary of the *in situ* major element compositions of BMS from five of the eclogite xenoliths included in this study are presented in Table 3, as measured by EPMA. In Figure 4 we compare the compositions from our study to BMS compositions of eclogite xenoliths at Roberts Victor reported by Gréau et al. (2013), and diamond inclusions at Roberts Victor (and globally) as reported by Deines & Harris (1995). Pyrrhotite, as quantitatively analysed in RV-IM-06 only, has a mean of 40.1 wt.% S and 56.8 wt.% Fe with minor Ni (2.43 wt.%). All other Fe-rich end-member sulphides measured were pyritic (52.1-53.2 wt.% or 65.9-66.8 at.% S; Table 3 and Fig. 4a). The precise composition of pentlandite and/or the Ni-rich sulphide end-members in the BMS was difficult to obtain due to the very fine lamellae intergrown with pyrite or pyrrhotite and the relative spot size of the EPMA. Thus, Ni-bearing sulphides in BMS are largely represented by the range of 'Py (± Ni)' in Figure 4b and Table 3. The major element compositions of the Fe-Ni-S sulphides in this study directly overlap the range of compositions from Gréau et al. (2013) – Figure 4b. The composition of chalcopyrite documented in our study more closely resemble the end-member composition of chalcopyrite than those recorded by Gréau et al. (2013) – Figure 4c. The concentration of Co is generally low (< 1 wt.%) for all sulphide end-members (Table 3).

Using ratios of major elements from our LA-ICP-MS data, we find that most BMS analysed in this study have Ni/(Ni+Cu+Fe) of < 0.3 (Fig. 5a) and this spans a similar range in compositions as determined for E-type (Ni/(Ni+Cu+Fe) < 0.18; Aulbach et al., 2012; McDonald et al., 2017) and P-type BMS inclusions

in diamonds (Ni/(Ni+Cu+Fe) 0.02 – 0.68; Bulanova et al., 1996; McDonald et al., 2017). However, all BMS in RV-IM-02 (and some from RV-IM-06 and RV-IM-15) have elevated Ni/(Ni+Cu+Fe) ratios > 0.30, more akin to P-type BMS inclusions in diamonds. Most BMS analysed in this study have Cu/(Cu+Ni+Fe) ratios equivalent to E-type diamond inclusions (0.005 – 0.30); however, BMS in RV-IM-02 fall at the lower end of this range (0.005-0.05) more similar to the P-type diamond inclusions (Fig. 5b).

### *3.3 BMS trace element composition*

Trace element data from *in situ* LA-ICP-MS analyses of BMS in the Roberts Victor eclogites are summarised in Table 4 and the full data set is provided in Supplementary Table E. A selection of time-resolved analyses (TRA) are presented in Supplementary Figure C.

The Roberts Victor eclogite xenolith BMS compositions are compared to BMS compositions in mid-ocean ridge basalts (MORB; Patten et al., 2013), BMS in mid-ocean ridge (MOR) peridotites (Alard et al., 2005), BMS inclusions in olivine from picritic MOR lavas (Savelyev et al., 2019), and BMS inclusions in E- and P-type diamonds (Bulanova et al., 1996; Aulbach et al., 2012; McDonald et al., 2017) in Figures 5 to 7. There is a broad correlation between total PGE and major element compositions of BMS (Fig. 5), such that higher Ni content BMS have higher total PGE abundances (Fig. 5a). With the exception of RV-IM-02, all samples from this study have low total PGE concentrations (< 100ppm, with most < 10 ppm) consistent with the compositional range of BMS inclusions in E-type diamonds. RV-IM-02 BMS are the notable exception, exhibiting compositions more akin to BMS inclusions in P-type diamonds (Fig. 5a-b). The eclogite BMS have a range of Cu concentrations (described by Cu/(Cu+Ni+Fe)) equivalent to those shown by MORB and both E-type and P-type diamond inclusions (Fig. 5b). There is no clear correlation between Cu content of BMS and total PGE, but we observe that RV-IM-02 BMS, with the highest total PGE content, has one of the lowest Cu/(Cu+Ni+Fe) ratios – Fig. 5b. There is no correlation between BMS compositions in Figure 5 according to whether the BMS are interstitial or included in garnet or clinopyroxene.

Chondrite-normalised Ni-PGE-Au-Re-Cu abundances (normalised after Fischer-Gödde et al., 2010) (Figure 6) show that within each xenolith the BMS loosely follow a single compositional trend. With the exception of RV-IM-02, the BMS mostly contain low total Ir-group PGE (IPGE; Os, Ir, Ru) < chondrite and fractionated PGE patterns such that Pd-group PGE (PPGE; Rh, Pt, Pd) > IPGE (Fig. 6). Further similarities in the plots are noted:

(i) *Type i*: RV-IM-01, RV-IM-05, RV-IM-15, and SS2 form a group with a U-shaped pattern for the IPGE and mostly negative Au anomalies and both negative and positive anomalies for Pt.

(ii) *Type ii*: RV-IM-03 and RV-IM-06 have this same basic pattern as (i) but extremely low PGE concentrations overall (mostly below detection limit, especially for the IPGE, Rh and Pt) and are relatively enriched in Au (> chondrite and lacking an apparent negative anomaly).

(iii) *Type iii*: RV-IM-17 has a similar U-shaped IPGE pattern as (i) but are notably enrichment in Pt and Pd (without these occurring as distinct peaks, unlike RV-IM-01, RV-IM-05, RV-IM-15, and SS2) and a systematic negative anomaly for Au.

(iv) *Type iv*: RV-IM-02 compositions are distinct from all other BMS analysed in this study, with elevated IPGE such that the chondrite-normalised multi-element patterns are relatively unfractionated and flat for the PGE, but with notable negative anomalies for Au and Re.

*Types i* to *iii* BMS are similar to the range in compositions shown by BMS inclusions in E-type diamonds and MORB (Fig. 6; Aulbach et al., 2012; Patten et al., 2013; McDonald et al., 2017; Savelyev et al., 2018). We also note that these resemble the compositional range of Gréau et al. (2008), although we cannot quantitatively compare our BMS compositions due to the authors presenting primitive mantle normalised diagrams and no accompanying published values. *Type iv* BMS are more comparable to P-type BMS diamond inclusions and overlap some mid-ocean ridge peridotite compositions (Fig. 6; Bulanova et al., 1996). Despite multiple laser measurements of RV-IM-02, our LA-ICP-MS data sample the only two BMS exposed on the surface of the thin section made from this xenolith and therefore

represent a relatively uncommon BMS signature across the eclogite xenolith suite as a whole, although we note that these resemble the IPGE compositions of 'Type I' BMS in Gréau et al. (2008).

We provide the mean of BMS composition for eclogites, based on all analyses in this study except from RV-IM-02, in Table 4. We suggest that our *Type i* and *Type iii* BMS compositions (i.e., the majority of our data) are equivalent to the 'Group 2' BMS compositions of Burness et al. (2020) while our *Type ii* BMS are equivalent to Burness et al. (2020) 'Group 1' with notable negative anomalies in Pt. However, our *Type iv* BMS are not recognised by the Burness et al. (2020) study, nor Gréau et al. (2008).

There is no discernible difference in PGE systematics between those BMS that are interstitial to the silicates compared to those that are included in garnet or clinopyroxene. There is no systematic difference between PGE, Au or Re abundance for the Cu- or Ni-rich BMS phases (Fig. 6 e.g., RV-IM-01, RV-IM-05, RV-IM-06, RV-IM-15 and RV-IM-17) although we note that the BMS in RV-IM-02 have the highest Ni concentration overall.

Distinct positive Pt anomalies in Figure 6 correlate with short-lived Pt peaks in the corresponding time-resolved analysis (TRA) for that analysis (e.g., Supplementary Figure C) caused by inclusion of a nano- or micro-nugget or a Pt-bearing platinum-group mineral (PGM). A similar correlation between peaks in Figure 6 and in TRA is also present for Au and to a lesser extent, Pd. The TRA show several Pd-Sb-Bi and Pt-Pd-Sb-Bi peaks indicting these are present as discrete PGM within the BMS, incorporated into some LA-ICP-MS line analyses. Platinum appears to be predominantly hosted within PGM. Based on the time-resolved spectra of all samples, we note many instances where Pd tracks Ni and/or Cu, and Re, Te and Se largely track Fe and S in the BMS. Arsenic is variable in the TRA, especially in pyrite, and there is no systematic association between As, Pt and Pd. The TRA-based observations are largely consistent with PGM search conducted by SEM (Supplementary Figure E) where rounded to elongate Pd (±Pt) antimonides and tellurides (±Bi, As), generally up to 1 μm in diameter and typically occurring at the rim of BMS, have been observed. In some cases, PGM in these samples have been identified as likely to be mertieite ($Pd_{11}(Sb,As)_4$ – $Pd_8(Sb,As)_3$). Platinum (±Pd) arsenides and Ni-

arsenides (significantly smaller than 1 μm and found within BMS) are also noted within some BMS. One electrum grain (< 1 μm) on the rim of the BMS was identified during SEM investigation.

Figure 7 shows bivariate trace element variations for BMS in Roberts Victor eclogite xenoliths, analysed by LA-ICP-MS, in comparison to BMS inclusions in E- and P-type diamonds. Distinct decoupling of many elements is apparent (e.g., Figs. 7a,c,e; PGE vs. S/Se, PGE vs. Au, and Te vs. Au) while others show moderate correlations (Fig. 7d; Te vs. Se). Further bivariate diagrams are presented in Supplementary Figure D.

The S/Se ratios (Fig. 7a and Supplementary Figure D and Table E) range from 1200 to 36840 with >50% of BMS having S/Se > 5500. Overall this range is similar to the bulk rock S/Se ratios of Gréau et al. (2013) of 500 to 9924 for Type I eclogites and from 16216 to 24277 for Type II eclogites. The measured S/Se is also generally higher than the primitive mantle S/Se ratio of 3300 (McDonough and Sun, 1995) and range in MORB S/Se (2682 to 4014; Patten et al., 2013), reflecting the dominance of pyrite in the Roberts Victor eclogite BMS assemblage (i.e., addition of S to the BMS assemblage via sulphidation to pyrite). The eclogite xenolith BMS display a similar range in S/Se to both P- and E-type diamond BMS inclusions (1260-22350 and 2540-13580, respectively; Bulanova et al., 1996; Aulbach et al., 2012; McDonald et al., 2017) – Fig. 7a. There is no correlation between S/Se ratio and total PGE abundance for specific xenoliths or the data set as a whole. Copper-rich BMS analyses (*Cu,Fe-(Ni) BMS*) tend to have higher S/Se ratios than Ni- or Fe-Ni-rich BMS analyses (except for RV-IM-06), reflecting their slightly lower Se concentrations – Table 4. The concentration of Se in the eclogite xenolith BMS data set ranges from 10 to 308 ppm and is higher (> 100 ppm) in SS2 and RV-IM-01 and low in RV-IM-17 (< 50 ppm) – Fig. 7b and Supplementary Table E. There is no correlation between Pd and Se (Fig. 7b) and individual BMS signatures show a range of Pd concentrations (up to 40 ppm) irrespective of Se concentration. This contrasts with the P-type diamond BMS inclusion data set of Bulanova et al. (1996) in which a positive correlation exists between Pd (7 to 50 ppm) and Se (17 to 301 ppm), and the E-type diamond BMS inclusion data that have generally very low Pd concentrations (0.03 to 10 ppm) but

423 a significant range of Se contents (29 to 150 ppm; Aulbach et al., 2012 and McDonald et al., 2017). The
424 range in MORB BMS (84 to 129 ppm Se, 0.04 to 45 ppm Pd; Patten et al., 2013) falls within the range
425 of our BMS data.

426 Concentrations of Au are mostly low (< 0.5 ppm) but some analyses show 0.5 to 1.8 ppm
427 (Supplementary Table E) and there is no apparent correlation between major element composition of
428 BMS and Au content (Table 4). Gold concentration is not correlated with total PGE (Fig. 7c); high Au
429 concentrations occur in BMS with low PGE, and vice versa. MORB BMS (Patten et al., 2013) and E-type
430 diamond BMS inclusions (Aulbach et al., 2012 and McDonald et al., 2017) exhibit similar
431 characteristics. Gold contents of P-type diamond BMS inclusions have not been reported (Bulanova et
432 al., 1996).

433 Tellurium and Se are weakly correlated (Fig. 7d), especially in RV-IM-01, and echoed by P-type
434 diamond BMS inclusions (Bulanova et al., 1996) and MORB BMS (Patten et al., 2013) to some extent.
435 Samples SS2 and RV-IM-05 also show a moderately positive correlation between Te and Se but with
436 significantly less variability of concentrations generally forming a tight cluster. Eclogite xenolith BMS
437 contain up to 63 ppm Te, although > 85% of BMS analyses have < 15 ppm. Tellurium and Au are not
438 correlated (Fig. 7e) and with the exception of RV-IM-01, the Roberts Victor eclogite xenolith BMS are
439 consistent with the range of compositions of MORB BMS (Patten et al., 2013) and BMS included in E-
440 type diamonds (Aulbach et al., 2012 and McDonald et al., 2017).

441 The eclogite xenolith BMS samples analysed in this study have low Os contents, from 0.01 to 0.20
442 ppm, with the exception of RV-IM-02, which hosts BMS with up to 13 ppm Os (Figure 7f, Table 4). The
443 $(Re/Os)_N$ ratio of our samples covers a wide range from 5.7 to 1357. Once again, RV-IM-02 is the
444 exception, with $(Re/Os)_N$ ratios < 1 as a result of the higher Os concentrations (> 10x chondrite) in
445 these BMS. Excluding the anomalous RV-IM-02, the Roberts Victor eclogite xenolith BMS compositions
446 are consistent with the Os contents and $(Re/Os)_N$ of a suite of E-type diamond BMS inclusions from
447 across Southern Africa (including Orapa, McDonald et al., 2017) and Diavik (Aulbach et al., 2012). RV-

IM-02 plots closer to P-type diamond BMS inclusion compositions (Simelane, 2004 – note that Bulanova et al. (1996) did not report Re data) and the mid-ocean ridge peridotite BMS compositions of Alard et al. (2005). The MORB BMS compositions of Patten et al. (2013) span a range of $(Re/Os)_N$ compositions from 3.2 to 77.5 (Fig. 7f). Based on Figure 7f, the range in $(Re/Os)_N$ appears to be largely controlled by the abundance of Os, rather than Re.

## 4. Discussion

### *4.1 Sulphur and the source of eclogitic BMS*

All xenoliths, apart from RV-IM-06, are dominated by interstitial BMS of a generally pyritic composition (with variable but low Ni and Cu concentrations – Table 3) with some chalcopyrite around the rim (Fig. 3d-f). In contrast, BMS in RV-IM-06 are largely included in silicates (89%, typically within garnet), rounded or with a polygonal shape, and pyrrhotite-dominated (with minor areas of pyritic composition), in comparison to the relatively minor interstitial BMS component of this xenolith which is pyrite-dominated. One BMS in RV-IM-01 was also pyrrhotite-dominated, rounded droplet-like in shape, and although interstitial, situated at the edge of what could be interpreted as an embayment in omphacitic clinopyroxene (Fig. 2a-c and Fig. 3a). Our observations of the dominance of pyrite in the BMS budget are consistent with the findings of Gréau et al. (2008, 2013) and Burness et al. (2020). Dale et al., (2009) studied gabbros and eclogites in the Zermatt-Saas ophiolite terrain and found that pyrrhotite is typically wholly or partially replaced by pyrite in eclogites (having been dominated by pyrrhotite in the gabbros). Dale et al. (2009) found that metamorphism of gabbros (with igneous pyrrhotite + pentlandite + minor chalcopyrite) to gabbroic eclogites (with pyrite, minor chalcopyrite and subsidiary pyrrhotite) coincided with a loss of Ni and Cu, a decrease in the metal/S ratio of sulphides preserved in eclogites, an overall reduction of bulk S concentration by 38%, and a reduction in the modal abundance of sulphides. They interpreted this as being caused by metamorphism from

gabbro to eclogite (i.e., 'eclogitisation') and highlighted the range in PGE geochemistry between gabbros, 'transitional gabbros' and gabbroic eclogites as evidence for progressive Pd-loss and Pt-gain throughout 'eclogitisation' (Dale et al., 2009). Notably, the concentration of IPGE appeared to be relatively unaffected during this metamorphism – Dale et al. (2009) interpreted this to reflect an inheritance of these elements from sulphides (and oxides) in the precursor gabbro, and therefore the immobility of IPGE during eclogitisation.

Based on petrography and the major element compositions of BMS, Gréau et al. (2013) identified two sulphide assemblages in Type I eclogites from Roberts Victor: pyrrhotite-pentlandite-chalcopyrite and (Ni)-pyrite-'smythite/violarite'-chalcopyrite. The latter assemblage was attributed to supergene alteration, via sulphidation of the sulphide 'primary' pyrrhotite-pentlandite-chalcopyrite (Gréau et al., 2013). However, our observations and data challenge the supergene interpretation of Gréau et al. (2013) based on: the ubiquity of the pyrite-bearing assemblage in all our xenoliths (even as inclusions within garnet and clinopyroxene); the co-existence of pyrite-bearing BMS with other interstitial BMS assemblages of pyrrhotite-pentlandite-chalcopyrite in the same xenolith; that pyrite- and pyrrhotite-bearing BMS assemblages may occur both interstitial to, and included within, silicates; and that PGE-rich *Type iv* BMS are pyrite-bearing. Given that Dale et al. (2009) demonstrated a transition from a pyrrhotite-dominated BMS assemblage to one that is pyrite-dominated may take place during metamorphism of oceanic crust (protolith) to eclogite during tectonic collision and subduction, we suggest that the prevalence of pyrite in the Roberts Victor xenoliths stems from the process of eclogitisation itself, rather than pyritisation by secondary supergene processes within the kimberlite host to the xenoliths. Our findings therefore also echo those of Evans et al. (2014) who identified $\delta^{34}S$ and cobalt zonation of pyrite and BMS assemblages in orogenic eclogites (Alpine and New Caledonia). Evans et al. (2014) interpreted these sulphide assemblages to have been modified and formed during the protracted history of devolatilisation and heterogeneous fluid flow throughout slab subduction and the earliest stages of exhumation, with remineralisation of the slab precipitating pyrite.

In the case of cratonic eclogite xenoliths sourced from the SCLM keel, protolith metamorphism is likely to be only one part of the protracted history of these rocks. Hence, in contrast to Dale et al. (2009) and Evans et al. (2014), we must also consider the role of metasomatism and partial melting within the SCLM in modifying the textures, mineralogy and BMS composition of eclogites: BMS geochemistry is likely to reflect the cumulative effects of some/all of these processes. In this way, we are presented with a similar paradigm to that of Kiseeva et al. (2017b) – that of the 'chicken or egg' dilemma of metamorphism and incipient mantle melting vs the involvement of speculative mantle metasomatism as an explanation for the geochemical and mineralogical features recorded in eclogite mantle xenoliths.

The generally IPGE-poor, PPGE-rich, Re-rich composition of BMS in this study (with the exception of RV-IM-02 *Type iv*) could be indicative of volatile-rich metasomatism adding Pd, Au, Re, S, as recorded in some peridotite mantle xenoliths (e.g., Alard et al., 2011; Delpech et al., 2012). The interstitial siting of the majority of Roberts Victor eclogite xenolith BMS could therefore favour a metasomatic origin; however the range in PGE systematics (Fig. 6) between our four BMS groupings (*types i* to *iv*) would therefore indicate that the composition of this metasomatic agent was variable (to account for both PGE-poor and PGE-rich signatures). This seems somewhat implausible when compared to the relatively consistent composition of metasomatic BMS in peridotite xenoliths (on a sample suite-by-suite basis) and the general absence of pyrite in the BMS assemblages of peridotite xenoliths. Notably, none of the BMS from Roberts Victor eclogite xenoliths (including RV-IM-02) show any correlation between total PGE and S/Se or Se. Thus the high S/Se ratio of BMS in eclogite xenoliths (echoed by that of BMS inclusions in E-type diamonds) may represent the increased S abundance in BMS due to the shrinking modal abundances of sulphides during eclogitisation (i.e., Dale et al., 2009; Evans et al., 2014). Hence we suggest that the trace element composition of eclogite xenolith BMS has largely been inherited from the protoliths of those eclogites (i.e., directly from the oceanic crust subducted during formation of the Colesberg Magnetic Lineament c. 2.9 Ga, the subsequent metamorphism of those rocks (similar to processes outlined by Evans et al., 2014), and cratonisation of the Kaapvaal and its

524 SCLM keel; Schmitz et al., 2004; Shu et al., 2013; Brey and Shu, 2018). Accordingly, we suggest that
525 the predominance of pyrite reflects the subduction and eclogitisation process itself (e.g., Dale et al.,
526 2009; Evans et al., 2014) rather than any subsequent metasomatic alteration within the cratonic SCLM
527 at very high $fS_2$ (cf. Burness et al., 2020), a general metasomatic overprint (cf. Gréau et al., 2013) or
528 supergene alteration (cf. Gréau et al., 2013).

529 Our interpretation is consistent with the petrological, compositional, and experimental-based
530 interpretations of Kiseeva et al. (2017b), which suggested that *in situ* melting of eclogites alone could
531 produce the geochemical signature of an enriched melt without the need for an external influence by
532 metasomatic fluids. Given their higher incompatible element abundances and lower solidus
533 temperatures than peridotites, such eclogites are a likely *source* of metasomatic fluids to surrounding
534 peridotites (Kiseeva et al., 2017b). The partial melting signature derived from the eclogite itself (e.g.,
535 Kiseeva et al., 2017b) is preserved as channels of 'spongy' diopsidic clinopyroxene. We observed
536 veinlets of pyrite branching off from interstitial BMS within these channels (e.g., Figs. 2d-e and 3d-f)
537 and acknowledge this as evidence for some degree of subsequent alteration and/or mobilisation of
538 the sulphides within these channels. The timing of this mobilisation is unclear – this could record an
539 *in situ* partial melting of the eclogites (e.g., Kiseeva et al., 2017b) or much later remobilisation of BMS
540 from decompression during transportation of the xenoliths to the crust in the Roberts Victor
541 kimberlite. Alternatively, this could indicate locallised thin section-scale redistribution of S, possibly
542 from fluid infiltration associated with metamorphism (Evans et al., 2014). Regardless of precise timing,
543 the extent of mobilisation appears to be limited and small scale (thin section-scale) and therefore we
544 suggest that this process had little effect on the metal budget of the eclogite BMS.

545

546 ***4.2 Characterising the eclogitic metal budget***

Overall, we identify four 'end-member' BMS compositions from the Roberts Victor eclogite xenoliths analysed in this study, based on their Ni-PGE-Au-Re-Cu systematics (Fig. 8):

- *Type i* – BMS from RV-IM-01, RV-IM-05, RV-IM-15, and SS2 have a wide range in Pt/Pd (0.002 to 72, mean 3.8) and variable but generally low Au/Pd (0.001 to 13, mean 0.76).
- *Type ii* – BMS from RV-IM-03 and RV-IM-06 have very low PGE concentrations overall (particularly Pt), low Pt/Pd (0.01 to 0.91, mean 0.26) and high Au/Pd (0.01 to 20, mean 5.6).
- *Type iii* – BMS compositions from RM-IM-17, similar to *Type i* with Pt/Pd ranging 0.49 to 1.9 (mean 1.2) and low Au/Pd (0.001 to 0.08, mean 0.02).
- *Type iv* – BMS compositions from RM-IM-02 which are characteristically PGE-enriched, particular for IPGE (with flatter PGE chondrite-normalised patterns), Pt/Pd ranging 1.0 to 39 (mean 8.7) and Au/Pd ranging 0.004 to 0.03 (mean 0.01).

*4.2.1 Eclogitic PGE signatures*

Of the eight xenoliths analysed in this study, five have low total PGE concentrations (typically < 10 ppm) in comparison with P-type BMS inclusions in diamonds (Figs. 5-7) or BMS in peridotite xenoliths (e.g., Luguet and Reisberg, 2016; Lorand and Luguet, 2016 and references therein). Three xenoliths (RV-IM-01, RV-IM-17 and RV-IM-02) have higher total PGE budgets than recognised in previous studies of Roberts Victor eclogites (Gréau et al., 2008; Burness et al., 2020) and are generally more enriched than MORB BMS (Patten et al., 2013) – Fig. 5. Of these, two samples (RV-IM-01 and RV-IM-17) have variable but generally high Pt and Pd concentrations (either recorded within BMS in solid solution or as nano- or micro-nuggets). Furthermore, BMS in RV-IM-02 (*Type iv*) have the highest total PGE concentrations (> 100 ppm) of all the xenoliths analysed and are some of the most enriched in eclogite xenoliths recorded so far globally; their IPGE/PPGE ratios and the overall shape of their chondrite normalised multi-element pattern are more akin to P-type diamond inclusions and mid-ocean ridge peridotites (Figs. 5-7 cf. Bulanova et al., 1996; Alard et al., 2005). These findings have significant implications for the PGE budget of the eclogitic SCLM.

572 *Type iv* BMS also resemble 'Group B' BMS in lherzolite xenoliths from the marginal cratonic setting of
573 Loch Roag (Scottish Outer Hebrides; Hughes et al., 2017); both have relatively high Ni concentrations
574 (Ni/(Ni+Cu+Fe) > 0.3) and we suggest that this is fundamental to their high total PGE abundance (>
575 100 ppm) and high IPGE (Fig. 6). However, we find it unlikely that *Type iv* BMS are directly derived
576 from P-type mantle themselves (cf. Aulbach et al., 2009) not least because *Type iv* BMS appear to be
577 comprised of pentlandite and Ni-pyrite. The BMS in RV-IM-02 are 200-400 μm in diameter, irregular
578 in shape (similar to the shapes of BMS in Fig. 3c-f), interstitial to silicates, and found in channels of
579 spongy diopsidic clinopyroxene (similar to those imaged in Fig. 2b). Hence *Type iv* BMS look similar to
580 any other interstitial BMS observed in the Roberts Victor eclogite xenolith suite (although no
581 significant chalcopyrite component was identified during petrographic inspection of this type of BMS),
582 and would likely be classed as 'metasomatic' in origin according to similar textures in peridotite
583 xenoliths (e.g., Aulbach et al., 2016; Lorand and Luguet, 2016).

584 Unlike BMS in peridotite xenoliths, for all of the eclogite xenolith BMS in this study (excluding *Type iv*),
585 we found no systematic differences between PGE or metalloid abundances (specifically Se and Te) vs.
586 the major element composition of each BMS analysis (Ni, Cu or Fe dominance). Thus, the eclogite BMS
587 budget differs significantly from peridotite BMS systematics (e.g., Lorand and Luguet, 2016 and Luguet
588 and Reisberg, 2016 and references therein) in that the BMS trace element compositions appear to be
589 more variable in eclogites. In particular, our data highlight that IPGE concentrations in eclogite xenolith
590 BMS are not uniformly low (e.g., up to 77 ppm in *Type iv* BMS) and that the total PGE (up to 223 ppm
591 in BMS) and PPGE (up to 167 ppm in BMS) budgets of eclogites may be higher than previously
592 reported.

593 *4.2.2 The presence of platinum-group minerals (PGM)*

594 We observe nano- and micron-scale PGM (typically ≤ 1 μm diameter) in the eclogite xenoliths,
595 including Pd-Pt antimonides, tellurides and arsenides spatially associated with BMS (Supplementary
596 Figure E). No IPGE-bearing PGM (e.g., Os-Ir alloys) were observed in our samples. The presence of

PPGE-bearing PGM (± Au) is corroborated by short-lived spikes for Pt, Pd and Au in TRA of LA-ICP-MS data (e.g., Supplementary Figure C). These LA-ICP-MS-based signals are integrated across the length of the laser line and each analysis may accommodate significant fluctuations in Pt (and Pd and Au), introducing an important nugget effect in the *in situ* BMS compositions. Conversely, significant negative anomalies in these elements on normalised plots (Fig. 6) reflect sample volumes where nano/micro-grains have not been intersected by the laser analysis, but nonetheless exist elsewhere within the BMS.

To our knowledge, the PGM we describe here are some of the first described occurrences in eclogite xenoliths and we herewith consider their genesis. In peridotite xenoliths, PGM tellurides and bismuthotellurides may be indicative of refertilisation (Eggler and Lorand, 1993; Lorand et al., 2010; Lorand and Luguet, 2016). Alternatively, PGM (such as the rounded to 'blocky' antimonides at the rim of BMS observed in our samples) may be interpreted as forming either by exsolution from a sulphide liquid before MSS and ISS formation (e.g., Peregoedova and Ohnenstetter, 2002; Sinyakova et al., 2016; Helmy and Botcharnikov, 2020; Anenburg and Mavrogenes, 2020) or after sub-solidus transformation (e.g., Fleet et al., 1993; Peregoedova, 1998; Holwell and McDonald, 2010). Kamenetsky and Zelenski (2020) also highlighted a mechanism whereby PGM may form via desulphidation of BMS during fluctuations in the environment of a magmatic plumbing system (e.g., changes in pressure, temperature and chemistry – FeO, $_{f}O_2$, $_{f}S_2$).

In contrast, the Pt,Pd-arsenide PGM (typically < 1µm and both rounded and irregular in shape) may be interpreted to represent secondary mineral phases related to localised extraction from BMS at low (non-magmatic) temperatures (e.g., Barkov and Fleet, 2004; Savelyev et al., 2018); thus the presence of PGM-arsenides may support the interpretation of supergene alteration in forming Ni-rich pyrite in eclogite xenoliths (Gréau et al., 2013). However, Gonzalez-Jimenez et al. (2020) highlighted that Pt-arsenides in SCLM-derived peridotite xenoliths may form directly as nanograins in BMS and therefore reflect PGM within the SCLM itself. Alard et al. (2011) and Delpech et al. (2012) further suggested a

link between Pt,Pd-arsenides, tellurides, and bismuthinides in Kerguelen and Montferrier peridotite xenoliths as forming from carbonate and phosphate-related mantle metasomatism. Whilst the precise timing of PGM formation in the Roberts Victor eclogites may not be answered definitively for now, the presence of PGM points to alternative mechanisms by which PGE and the precious metal budget of eclogitic SCLM may become mobilised during partial melting, metasomatism and major magmatic events impinging upon the cratonic keel.

*4.2.3 Tellurium, selenium and gold*

Tellurium and Se were detected in all eclogite BMS analysed in this study, but generally occur at low concentrations (typically Te < 15 ppm and Se < 150 ppm). This is similar to Te and Se concentrations in BMS inclusions in E-type diamonds (Aulbach et al., 2012; McDonald et al., 2017) and many BMS compositions in peridotite xenoliths (< 10 ppm Te, e.g., Lorand and Alard, 2010). Although Te and Se are generally thought of as coupled chalcophile metalloids in mantle petrology, their chemical behaviour is typically decoupled due to the heterogeneous presence of nano/micro-scale tellurides (e.g., Lorand and Alard, 2010; König et al., 2012; Brenan, 2015; Harvey et al., 2015; Luguet et al., 2015). However, we see a broad correlation between Te and Se in BMS on a sample-by-sample basis for some of the eclogite xenoliths analysed in this study (Fig. 7d – e.g., RV-IM-01, SS2, RV-IM-02), and together with evidence of coupled behaviour in TRA (e.g., Supplementary Figure C for RV-IM-01) we suggests this reflects incorporation of both of these elements in solid solution within BMS, in addition to nano/micro-scale Te-bearing PGM. There is no correlation between Te and Au (Fig. 7e) and this corroborates with an absence of Au-telluride nano/micro-grains associated with BMS in our eclogite xenoliths. The apparently low Au concentrations in BMS may indicate Au decoupling from the sulphide budget with 'missing' Au budget accommodated by a non-sulphide mineral phases hosted within silicates, similar to the nano-inclusions of Au found in the strained (deformed and recrystallized) crystal margins of olivine in Pyrenean lherzolites (Ferrais and Lorand, 2014), thus introducing a nugget effect in the sampling. The presence of a Au-bearing nano/micro-mineral phase hosting the 'missing'

Au budget is supported by our finding a rounded grain of electrum (Au,Ag) in association with Ni-pyrite observed in our eclogite samples.

The concentration of Pd and Se in BMS inclusions in P-type diamonds (Bulanova et al., 1996) and some bulk rock compositions of peridotite xenoliths (e.g., Harvey et al., 2015) are positively correlated, suggesting similar chalcophile behaviour of the two elements such that Se concentration may be used as a proxy for total PGE abundance. Hence, PGE-rich samples would be expected to have lower mantle-like S/Se ratios (primitive mantle S/Se = 3300 (McDonough and Sun, 1995) vs. 3000 in Pyrenean peridotites (Lorand & Alard, 2010) and chondrite S/Se = 2500 ± 150 (Dreibus et al., 1995)). The concentration of Se in BMS analysed in this study (10 to 308 ppm) overlaps with the composition of peridotitic BMS and MORB BMS (Patten et al., 2013) but have a much wider range in Se abundance (up to 308 ppm). This is similar to the range in Se abundances reported by Burness et al. (2020) in Roberts Victor and Jagersfontein eclogites (49 to 588 ppm) and could reflect the generally lower Ni and S-rich composition (typically pyritic) of the eclogitic BMS in this study (Fig. 5a), in comparison to a mean of 133 ppm in pentlandite, 136 ppm in chalcopyrite and 26 ppm Se in pyrite from Pyrenean peridotites (Lorand and Alard, 2010).

Using bulk geochemistry, some mantle xenolith studies have demonstrated that Se may be mobilised during supergene alteration (e.g., Gréau et al., 2013; Harvey et al., 2015). However, *in situ* BMS analysis of a 'pristine' eclogite xenolith by Gréau (2011) has shown that the primary eclogitic S/Se ratio may be superchondritic (6000-10,000), similar to metasomatic peridotite-hosted BMS (e.g., Lorand et al., 2003; Alard et al., 2011) and distinct from sulphides in kimberlites (> 90,000) – Gréau et al. (2013). Given that 87% of our BMS analyses have S/Se ratio < 10,000, we therefore suggest that the trace element signature of eclogitic BMS is still largely representative of their metal budget when *in situ* in the Kaapvaal SCLM, despite alteration to the pyritic assemblages now prevalent in the xenoliths.

### *4.3 Implications for metallogenesis and the metal budget of mantle-derived mafic magmatic systems*

Models for the source of chalcophile metals in mineralisation linked to mafic magmatic systems typically refer to peridotite partial melting in which BMS in the mantle source are interstitial to the silicate minerals and are assumed to be homogenous in composition (Naldrett (2011)). During partial melting, the most fusible minerals in the source melt first (e.g., BMS, clinopyroxene and garnet) and as partial melting continues, more BMS are incorporated into the silicate melt until the BMS budget of the residue is depleted. Given the strongly chalcophile behaviour of the PGE, and their extremely high partition coefficients between sulphide minerals and silicate melt (e.g., from $4x10^5$ (Ru) to 2-3x $10^6$ (Ir, Pt); Mungall and Brenan, 2014) any BMS left in the mantle source will suppress the uptake of PGE into the silicate melt. However, once partial melting exhausts the BMS budget of the source, the full PGE budget is transferred into the melt. This paradigm is the basis for models describing the fertility of mantle-derived magmas that feed mineralising systems and thus ore deposit models (Naldrett, 2011), although the significance of an incongruent melting scenario has more recently gained momentum (e.g., Holwell et al., 2019; Choi et al., 2020). However, different populations of BMS exist in the mantle and that their various textural settings (interstitial vs included, what silicate mineral assemblage they are associated with, peridotitic vs eclogitic source lithology for partial melting in the mantle, etc) mean that BMS (and the PGE budget thereof) may be unevenly vulnerable to partial melting. For example, given the substantially lower solidus temperatures for eclogites in comparison to peridotites (Yaxley and Brey, 2004; Spandler et al., 2008; Green et al., 2010; Herzberg and Zhang, 1996), eclogite is more likely to undergo extensive partial melting during large magmatic events and therefore eclogite-hosted BMS and its metal budget may be particularly susceptible to mobilisation. Indeed, it is plausible that sulphide may even be physically entrained as droplets within melts derived from such extensive eclogitic partial melting.

#### *4.3.1 An eclogitic source component in parental magmas of the Bushveld Complex?*

696 Southern Africa records several major large igneous provinces (LIP) throughout its history and the c.
697 2.05 Ga Bushveld LIP (Zeh et al., 2015) in particular hosts many of the world's most important
698 orthomagmatic PGE-Ni-Cu ore deposits (e.g., Naldrett, 2011). The source(s) of magmas that fed the
699 Bushveld magmatic event and the controls on the metallogenic signature of this LIP remain debated.
700 Several models now evoke extensive plume-related partial melting of the mantle (Hatton, 1995), with
701 varying proportions of SCLM-derived magmas vs crustal contamination to explain geochemical facets
702 of igneous rocks of the Bushveld LIP (e.g., Harris et al., 2005; Barnes et al., 2010; Zirakparvar et al.,
703 2014, 2019; Zeh et al., 2015, 2020; Wilson et al., 2017). Bushveld-aged diamond-hosted BMS
704 discovered at Venetia and Premier (Richardson & Shirey, 2008) demonstrate a link between LIP events
705 and the formation of some generations of diamonds and mantle BMS. Although contentious, based
706 on Re-Os isotopic evidence from diamond BMS inclusions (Richardson & Shirey, 2008) and Sr-isotopic
707 evidence from quenched ultramafic units in the Bushveld Complex itself (Wilson et al., 2017) some
708 authors have linked the formation of the Bushveld Complex to varying components of partial melting
709 of eclogitic rocks in the SCLM underlying the Complex (e.g., Richardson & Shirey, 2008; Zeh et al.,
710 2015). Richardson & Shirey (2008) put forward a model whereby parental Bushveld magmas were
711 derived from approximately 40% SCLM melting with a 10% eclogitic component for the more
712 magnesian Lower Zone (i.e., a total of 4% eclogitic component to the parental magma), to 75% SCLM
713 melting with 70% eclogitic component for the more aluminous character of the Main Zone. On the
714 face of it, such a significant eclogitic signature in these parental Bushveld magma models (i.e.,
715 Richardson & Shirey, 2008; Zeh et al., 2015) appear to conflict with the average proportion of eclogitic
716 rocks in the cratonic lithosphere which is generally agreed at 1 to 4 % by volume (Schulze, 1989;
717 McLean et al., 2007), consistent with seismic evidence ruling out large clusters of eclogite material in
718 the Kaapvaal SCLM (James et al., 2004). Yet, despite this, eclogitic xenoliths and inclusions in diamonds
719 are disproportionally abundant entrained in some kimberlite-derived magmas.

720 Until recently, due to the lack of data on the PGE abundances in cratonic eclogites available in
721 published literature, it was not possible to quantitatively assess if the PGE budget of eclogitic BMS

could contribute significantly to the metal basket of mafic magmatic systems and PGE-enriched intrusions, such as the layered mafic portion of the Bushveld LIP (Rustenburg Layered Suite; RLS). We address this by using the measured BMS compositions in our Roberts Victor eclogite xenoliths to model the chalcophile element budget of magmas produced by partial melting of an eclogitic source in the SCLM. We compare this to the parental magma compositions hypothesised to have fed the layered mafic RLS of the Bushveld in order to comment on the viability of the aforementioned models (e.g., Richardson and Shirey, 2008) from a metallogenic perspective.

We modelled the chalcophile (Ni, PGE, Au, Cu) and Re element composition of silicate melts derived from partial melting of Roberts Victor eclogite BMS (as measured in this study) – see Figures 9 and 10 and Supplementary Figure F. The details of the modelling method, including partition coefficients and starting compositions, are provided in the Supplementary Information. In each case, we compare the modelled composition of eclogite-derived silicate melt to the composition of the parental magmas of the RLS. The RLS parental magmas compositions are based on quenched contact rocks (including some sills) from the margins of the Lower and lower Critical zones (B1: tholeiitic basalt with Mg# 71), upper Critical Zone (B2: tholeiitic basalt with Mg# 55), and Main Zone (B3: tholeiitic basalt with Mg# 62) – see Barnes et al. (2010).

We assume that prior to melting, BMS present in the eclogites would likely be solid, based on P-T estimates of 1150°C and 5-6 GPa for sample SS2 (Kiseeva et al., 2017b) and in line with estimates of other Roberts Victor xenoliths being derived from > 140 km (e.g., Burness et al., 2020) and thus pressures > 3 GPa, with a geothermal gradient of approximately 45 $mWm^{-2}$ (Miller et al., 2016). If the eclogite contains carbon (which is likely given their oceanic crust origin), then the sulphide solidus at 3 GPa is approximately 1125°C, and 1250°C at 5-6 GPa (Zhang et al., 2015). Accordingly, we modelled the behaviour of chalcophile elements as partitioning between only two phases: 'sulphide' and a liquid silicate melt. Given the strong chalcophile behaviour of the PGE, as reflected by their extremely high Nernst partition coefficients (Mungall and Brenan, 2014), essentially all of the BMS in the source ( >

747 99%) must be melted and incorporated into the silicate partial melt in order for it to have any tenable
748 PGE budget (see Supplementary Figure F); thereafter all modelling assumed that 100% of the BMS was
749 melted out of the mantle source and added to the silicate magma formed (Figs. 9-10). This is especially
750 feasible in the case of an eclogitic source where, although the sulphide would be expected to melt
751 before the silicates (Zhang et al., 2015), the silicates themselves are highly fusible.

752 By modelling partial melting of an eclogite source with each of the four end-member BMS
753 compositions in this study, we produced silicate melts of distinct compositions (Figure 9a). Notably,
754 melts derived from a *Type iv* eclogite source (i.e., with BMS of RV-IM-02 composition) are over
755 endowed for all PGE in comparison to all Bushveld parental magmas. Similarly, melts solely derived
756 from a *Type iii* eclogite source are relatively Pt and Pd enriched. Melts derived from a *Type ii* eclogite
757 source (i.e., with BMS of RV-IM-03 and RV-IM-06 composition) are depleted relative to the Bushveld
758 parental magmas, especially for Pt. However, melts derived from a *Type i* eclogite source, and indeed
759 those derived from a mean composition for Roberts Victor BMS (calculated based on all BMS analyse
760 in this study, excluding the rare PGE-enriched RV-IM-02 BMS) produce melts with chalcophile
761 abundances similar to the composition of Bushveld parental magmas B1, B2 and B3. In Figure 9b, we
762 mix *Type i* and *Type iv* BMS in various proportions and demonstrate that the PGE-rich composition of
763 *Type iv* (RV-IM-02) is capable of significantly enriching the total PGE content of a silicate magma
764 produced during partial melting, even if only present in very small proportions (e.g., 5% *Type iv* in the
765 total BMS budget).

766 The variation in eclogite BMS compositions relative to Bushveld parental magmas is further
767 demonstrated in Figure 10. Partial melts derived from an eclogite source with complete BMS melting
768 span the range of total PGE concentrations of the Bushveld parental magmas (Fig. 10a), including the
769 B2 upper Critical Zone composition that is suggested to be fundamental to the metal budget of the
770 main mineralised reefs of the RLS, including the UG2, Merensky Reef, Bastard Reef and Platreef.
771 Furthermore, the Pt/Pd and Ni/Cu ratios of these eclogite-derived melts are close to those found in

772 the Bushveld parental magmas (Fig. 10a-b). It has been suggested that the observed radiogenic Os
773 signatures of the Bushveld reefs were derived directly from the an eclogitic component in the SCLM,
774 on the basis of the high initial $^{187}Os/^{188}Os$ of BMS included within 2.05 Ga diamonds (Richardson &
775 Shirey, 2008) and their similarity to the Os-isotopic compositions of PGM and chromitites in the upper
776 Critical Zone of the RLS in the Bushveld – i.e., the stratigraphic point in this layered intrusion where
777 the main PGE-mineralised reefs occur ($^{187}Os/^{188}Os$ ranging 0.11 to 0.19 – Hart and Kinloch, 1989;
778 McCandless and Ruiz, 1991; Schoenberg et al., 1999; Coggon et al., 2012). At the time of writing, there
779 is no published Re data for the Bushveld parental magmas (B1-3 and UM), hence we cannot make a
780 direct comparison between our eclogite-derived model melts and Re/Os of the Bushveld magmas.
781 However, comparison to the estimated 'Bushveld primary melt' of McCandless & Ruiz (1991) (Re/Os
782 = 28) again demonstrate that the range of eclogitic compositions also reasonably covers this overall
783 Bushveld signature (Fig. 10c).

784 In summary, our chalcophile element models demonstrate that partial melting of SCLM eclogites may
785 be capable of enhancing the metal basket of the asthenosphere-derived parental magmas of the
786 Bushveld LIP. In this sense, SCLM eclogite-derived partial melts may be as PGE-fertile as
787 asthenospheric peridotite-derived melts as a consequence of the variable IPGE-rich and PPGE-rich
788 BMS populations that eclogites contain and the fusible nature of this rock type. Thus, an eclogitic
789 component to the Bushveld parental magmas is supported both isotopically (Richardson & Shirey,
790 2008; Zirakparvar et al., 2014, 2019; Zeh et al., 2015, 2020) and metallogenically (this study).

791

792 **5. Conclusions**

793 1. The BMS are dominated by assemblages bearing pyrite (with variable Ni and Cu content),
794 although some pyrrhotite-bearing BMS are also observed. We interpret the dominance of
795 pyrite to reflect metamorphism of the original pyrrhotite-dominated igneous assemblage of

796 the protolith to the eclogites (in line with interpretations of Dale et al. 2009). Accordingly, the
797 BMS budget was introduced into the SCLM via ancient subduction (i.e., oceanic crust
798 subducted during formation of the Colesberg Magnetic Lineament c. 2.9 Ga and the
799 cratonisation of the Kaapvaal and its SCLM keel; Schmitz et al., 2004; Shu et al., 2013; Brey
800 and Shu, 2018). Whilst some subsequent modification of BMS may have occurred (e.g., Gréau
801 et al., 2013) we highlight that the predominance of pyrite reflects the eclogitisation process
802 itself rather than metasomatic alteration at high $fS_2$ (cf. Burness et al., 2020).
803 2. S/Se ratios of the majority of BMS are < 10,000, in line with the superchondritic S/Se (6000 to
804 10,000) of 'pristine' eclogite xenoliths by Gréau (2011). Hence, the trace element signature of
805 eclogitic BMS is largely representative of their metal budget when *in situ* in the Kaapvaal SCLM
806 keel and we suggest that the trace element composition of eclogite xenolith BMS has chiefly
807 been inherited from the oceanic crustal protoliths of the eclogites.
808 **3.** We recognise four 'end-member' compositions (*types i* to *iv*) in the Roberts Victor eclogite
809 xenoliths, distinguished by total PGE abundance and Pt/Pd and Au/Pd ratios. Whilst the
810 majority of these have low total PGE concentrations (typically < 10 ppm), *Type iv* BMS are
811 highly enriched in PGE (> 100 ppm total PGE). Crucially, *Type iv* BMS have the highest recorded
812 PGE abundances in eclogite so far, with a distinctive IPGE-enriched composition and thus
813 indicate that the PGE budget of the eclogitic SCLM may be substantially higher than previously
814 reported.
815 4. We observe PGM in the Roberts Victor eclogite xenoliths, including nano- and micron-scale
816 Pd-Pt antimonides, tellurides and arsenides spatially associated with BMS. To our knowledge,
817 these are some of the first PGM documented in eclogite mantle xenoliths. The PGM may have
818 exsolved from BMS during cooling, however these may also be formed during modification of
819 the BMS (pyritisation).
820 5. Based on isotopic evidence from diamond inclusions and the Rustenburg Layered Suite,
821 authors have previously proposed that partial melting of eclogites in the SCLM have directly

822 contributed to the Bushveld parental magmas (e.g., Richardson & Shirey, 2008; Zeh et al.,
823 2015). However, until recently it was not possible to quantitatively assess if the PGE budget
824 of eclogitic SCLM could contribute significantly to the metal basket of mafic magmatic systems
825 and PGE-enriched intrusions. We modelled the chalcophile (Ni, PGE, Au, Cu) and Re element
826 composition of silicate melts derived from partial melting of Roberts Victor eclogite BMS.
827 Using the mean of *Type I, ii, and iii* BMS compositions, we demonstrate that incorporation of
828 SCLM eclogites (via partial melting) into ascending asthenosphere-derived magma is not
829 detrimental to the metallogenic budget of that magma. Crucially, by incorporating just 5% of
830 *Type iv* BMS into our total eclogitic BMS budget, we find that eclogitic SCLM-derived partial
831 melting could in fact enhance the metal basket of ascending asthenosphere-derived partial
832 melts.

***Acknowledgements***

*Steve Pendray and Joe Pickles are thanked for sample preparation and lab support, respectively. The research in Oxford University was financially supported by NERC grant NE/L010828/1 to ESK. VSK acknowledges funding by the Russian Science Foundation grant no. 16-17-10145. IMcD acknowledges support from the Natural Environmental Research Council (NERC) under tellurium and selenium cycling and supply grant NE/M010848/1. The authors thank Marek Locmellis, Marco Fiorentini and Steve Barnes for their constructive and thorough reviews, and José Maria Gonzalez-Jiménez for his editorial handling of the paper.*

841 **Figure captions**

842 **Figure 1** – Map of southern Africa showing location of Roberts Victor (RV) kimberlite relative to the
843 Kaapvaal and Zimbabwe cratons and adjoining orogenic belts, the Colesberg Magnetic Lineament, a
844 selection of other kimberlite localities, the Transvaal Supergroup, the Bushveld Complex and the
845 Molopo Farms Complex in Botswana (of the same age as the Bushveld Complex, part of the same
846 Large Igneous Province). Acronyms include Pietersberg block (PB), Kimberley block (KB),
847 Witwatersrand block (WB), Swaziland block (SB). The double line in the West delineates the edge of
848 the Kalahari Craton (consisting Kaapvaal Craton, Zimbabwe Craton, Limpopo Belt and the Kheis – Okwa
849 – Magondi Belt).

850 **Figure 2** – QEMSCAN® false colour mineral maps of RV-IM-01 using field scan technique (see
851 Methods). (a) Whole section scan (at 10 µm resolution) showing relationships between garnet and
852 clinopyroxene (Na-rich, omphacite) with network of 'spongy' Na-poor clinopyroxene (labelled 'Ca Ma
853 (Fe Al) silicates), albite, K-feldspar, biotite and minor chlorite. A grain of phlogopite (± chlorite) is seem
854 on the margin of the xenolith. (b) A 1 µm resolution field scan of a rounded BMS (with chalcopyrite
855 rim and intergrown lamellae of pyrrhotite and pentlandite with minor pyrite) sited within a channel
856 of 'spongy' and intergrown Na-poor and Na-rich clinopyroxene with albite at the margin of two Na-
857 rich (omphacite) clinopyroxene crystals. (c) Same area as (b) but highlighting the texture of the BMS
858 and albite in the channel. (d) A 1 µm resolution field scan of a blocky BMS grain at the margin of a
859 garnet and Na-rich clinopyroxene. Notice the Na-poor clinopyroxene (labelled Ca Ma (Fe Al) silicates)
860 along fractures and channels into the Na-rich clinopyroxene. (e) Same area as (d) but highlighting the
861 texture of the BMS and its relationship with pyrite and sphalerite intergrown in the channels with K-
862 feldspar and Na-poor clinopyroxene.

863 **Figure 3** – Reflected light photomicrograph and BSE images of BMS from the Roberts Victor eclogite
864 xenoliths. (a) Reflected light photomicrograph of rounded BMS in RV-IM-01 in a channel of 'spongy'
865 Na-poor clinopyroxene intergrown with minor K-feldspar at the crystal boundary of primary Na-rich

clinopyroxene (omphacite). This is the same area as pictured in Fig. 2(b-c) and comprises pyrrhotite with lamellae of pentlandite and a rim of chalcopyrite. Pock-marks on the surface are the result of polishing and slight tarnishing. (b) BSE image of three rounded BMS in SS2. The BMS towards the top of the image is an embayment in Na-rich clinopyroxene surrounded by a ring of 'spongy' Na-poor diopsidic clinopyroxene (labelled 'Di'). The other two BMS in this image are interstitial, surrounded by channels of spongy 'secondary' accessory minerals. A rounded inclusion of garnet (Grt) is present within the main primary Na-rich clinopyroxene (CPX). (c) BSE image of blocky BMS from RV-IM-06 composed entirely of lamellae of pyrite and Ni-rich pyrite (appear striated in image, labelled as mss). Blocky Ni-rich pyrite occur around the rim . The BMS is interstitial to garnet. (d) BSE image of irregularly shaped BMS in RV-IM-15 interstitial to garnet and Na-rich clinopyroxene (and within a channel of intergrown Na-poor clinopyroxene, K-feldspar and biotite). The BMS is partially oxidised (labelled 'ox') and largely composed of lamellae of pyrite and Ni-rich pyrite (labelled mss). Chalcopyrite occurs at the rim through the centre of the grain. (e) Elongate BMS in SS2 similar to (d) and situated as an embayment in Na-rich clinopyroxene with a channel of intergrown Na-poor clinopyroxene and K-feldspar (on the right of the BMS and embayment). Notice that pyrite has become intergrown with silicates in the channel. (f) Bleb-like BMS in SS2 interstitial to garnet and Na-rich clinopyroxene with a nearby channel of Na-poor pyroxene. Pyrite and chalcopyrite have mobilised along these channels forming thin stringers off the rim of the main BMS grain. The BMS grain has the same characteristics as the other BMS presented here (lamellae of pyrite and Ni-rich pyrite (labelled 'mss') with chalcopyrite around the margins and in some lines in the grain). Abbreviations are chalcopyrite (Cp), pyrite + Ni-rich pyrite (mss), Na-rich clinopyroxene (CPX), Na-poor clinopyroxene (Di), garnet (Grt), partial oxidation of sulphides (ox).

**Figure 4** – Major element chemistry of BMS analysed by EPMA. (a) Histogram of S contents (in at.%) of BMS. Note that SS2-1 and SS2-4 refer to the same eclogite xenolith (SS2, from Kiseeva et al., 2017b) but different polished thin sections. (b) Fe– Ni(+Co)–Cu ternary diagrams showing eclogite xenoliths from this study in comparison to Roberts Victor eclogite xenoliths from Gréau et al. (2013) and BMS

inclusions in diamonds (Deines & Harris, 1995). (c) Cu–Fe–S diagram for chalcopyrite analysed during this study in comparison to compositions from Gréau et al. (2013) and end-member chalcopyrite. Abbreviations are chalcopyrite (Cp), pyrite with varying Ni content (Py ± Ni), pyrrhotite (Po), pentlandite (Pn), smythite-violarite (Smy-Vi) E-type diamond inclusion (E-Di) and P-type diamond inclusion (P-Di).

**Figure 5** – Scatter plots for total PGE *vs.* various indicators of BMS major element composition and/or dominant end-member sulphide mineral – (a) Ni/(Ni+Cu+Fe) and (b) Cu/(Cu+Ni+Fe). All Roberts Victor eclogite xenoliths (RV-IM-xx and SS2) have been plotted in comparison to BMS inclusions within eclogitic (E-type) and peridotitic (P-type) diamonds (data for Orapa (E-type, McDonald et al., 2017), Diavik (E-type, Aulbach et al., 2012), and Mir and Udachnaya (P-type, Bulanova et al., 1996)), BMS in mid-ocean ridge basalts (MORB) from Patten et al. (2013), and BMS inclusions in MORB (picritic lavas) from Savelyev et al. (2018).

**Figure 6** – Chondrite-normalised PGE and Au spidergrams of BMS from the Roberts Victor eclogite xenoliths (RV-IM-xx and SS2), with comparison plot of base metal sulphide (BMS) inclusions within eclogitic (E-type) and peridotitic (P-type) diamonds (data from McDonald et al., 2017; Aulbach et al., 2012 and Bulanova et al., 1996), BMS in mid-ocean ridge basalts (MORB) from Patten et al. (2013), BMS inclusions in MORB (picritic lavas) from Savelyev et al. (2018), and BMS in mid-ocean ridge (MOR) peridotites from Alard et al. (2005). All diagrams have been normalised to chondrite values from Fischer-Gödde et al. (2010). Note that the eclogite xenolith data (this study) have been plotted according to the corresponding Ni, Cu and Fe contents per LA-ICP-MS analyses to investigate the effect of BMS major element composition on PGE-Au-Re contents. Thus, the following categories were used: *Fe-(Ni,Cu) BMS* for analyses where both Ni and Cu occurred at < 10 wt.% each, *Ni,Fe-(Cu) BMS* for analyses with ≥ 10 wt.% Ni and < 10 wt.% Cu, and *Cu,Fe-(Ni) BMS* for analyses with ≥ 10 wt.% Cu and < 10 wt.% Ni. One analysis contained almost equal abundances of Ni and Cu (approximately 10 wt.% of each) and has been labelled *Ni,Cu,Fe BMS*.

**Figure 7** – Bivariate trace element diagrams for BMS measured by LA-ICP-MS. (a) total PGE *vs.* S/Se, (b) Pd *vs.* Se, and (c) S/Se *vs.* Au. (c) and (d) explore range of Te concentrations with Se and Au, respectively. (e) chondrite-normalised Re/Os ratio ($(Re/Os)_N$) *vs.* Os. All Roberts Victor eclogite xenoliths (RV-IM-*xx* and SS2) have been plotted in comparison to BMS inclusions within eclogitic (E-type) and peridotitic (P-type) diamonds using data from McDonald et al., (2017), Aulbach et al. (2012) and Bulanova et al. (1996), BMS in mid-ocean ridge basalts (MORB) from Patten et al. (2013), and BMS inclusions in MORB (picritic lavas) from Savelyev et al. (2018). Additional Re and Os data from Richardson et al. (2001, 2004), McKenna (2001) and Simelane (2004) for diamond inclusions, and BMS in mid-ocean ridge (MOR) peridotites from Alard et al. (2005).

**Figure 8** – Summary of chondrite-normalised PGE and Au spidergrams showing four main compositional groups of BMS from the Roberts Victor eclogite xenoliths in this study: Types *i*, *ii*, *iii* and *iv*. Comparison is made to Burness et al. (2020).

**Figure 9** – Trace element modelling of batch partial melting of Roberts Victor eclogite BMS as shown by chondrite normalised (Fischer-Gödde et al., 2010) Ni, PGE, Au, Re and Cu spidergrams for silicate melts generated by (a) different starting compositions of mantle BMS (as defined by the four end-member BMS compositions identified for Roberts Victor, se Section 4.1) and (b) mixtures of BMS end-members. In all models, we have assumed 100% BMS extraction from the source during melting and used an initial starting proportion of 0.5% (by volume) of BMS in the eclogite source. Note that in (a), a mean Roberts Victor BMS composition have been calculated from LA-ICP-MS data for all Roberts Victor eclogite xenoliths analysed in this study, excluding the PGE-rich samples of RV-IM-02. In (b), end-members *i* (based on mean from BMS in RV-IM-01, RV-IM-05, RV-IM-15 and SS2) and *ii* (based on mean BMS composition from RV-IM-02) are mixed in ratios of 50:50, 80:20 and 95:5 (*i : ii*). All modelled silicate melt compositions (coloured lines with diamond symbols) are plotted in comparison to the parental magma compositions for the Bushveld (B1-3 and UM) from Barnes et al. (2010), plotted as grey and black lines with circle symbols).

**Figure 10** – Trace element ratio and total PGE plots of melts derived from end-member Roberts Victor eclogite xenolith BMS (calculated by the same method as Fig. 9a) in comparison to Bushveld parental magmas (Barnes et al., 2010). (a) Pt/Pd ratio vs total PGE concentration, (b) Pt/Pd ratio vs Ni/Cu ratio, and (c) Pt/Pd ratio vs Re/Os ratio. Note that in (c), the lack of Re data for the Bushveld parental magmas (at the time of writing) mean that we cannot make a direct comparison to B1-3 and UM for Re/Os. Instead we use the 'Bushveld primary melt' of McCandless & Ruiz (1991). Also shown are the Re/Os ratios of gabbroic and basaltic eclogites from the Zermatt-Saas ophiolite terrain (Dale et al., 2009) in lilac lines, the range of Re/Os ratios of BMS in eclogite xenoliths from Diavik (Slave Craton) (Aulbach et al., 2009) as a grey bar, the chondritic composition of Fischer-Gödde et al. (2010) (black circle), and the composition of Pyrolite from McDonough and Sun (1995) (grey circle).

**Table captions**

**Table 1 –** Characteristics of mantle eclogite samples. All eclogites used in this study are classed as type I – see text for details. Texture classifications based on McGregor and Carter (1970). *See Kiseeva et al. (2017b) for further details on silicate chemistry and textures.

**Table 2 –** Relative proportions of base metal sulphides (by area %) analysed by QEMSCAN.

**Table 3 –** Summary of major element compositions of sulphides in Roberts Victor eclogite xenoliths analysed *in situ* by EPMA.

**Table 4 –** Summary of trace element compositions of analysed *in situ* by LA-ICP-MS. Full dataset in Supplementary Material (including all major elements as measured by LA-ICP-MS). * for Ru, Rh and Pd indicates abundances are reported for the element and have been corrected for isotope overlaps with argide species. The following categories were used: *Fe-(Ni,Cu) BMS* for analyses where both Ni and Cu occurred at < 10 wt.% each, *Ni,Fe-(Cu) BMS* for analyses with ≥ 10 wt.% Ni and < 10 wt.% Cu, and *Cu,Fe-(Ni) BMS* for analyses with ≥ 10 wt.% Cu and < 10 wt.% Ni. Sample SS-2 had a restricted range of BMS major elements compositions equivalent to pyrite with variable but low Ni and Cu concentrations and has therefore been labelled *Py (± Ni,Cu)*.

** Se concentration based on $^{82}Se$ isotope for these samples (as opposed to $^{77}Se$ for all others).

**Table 5 –** Count (*n)* of interstitial vs included (and embayed) BMS in eclogite xenoliths from this study and percentages of each per sample. No data available for RV-IM-01 and RV-IM-17.

**Supplementary material**

**Table A –** Mineral association data for samples analysed by QEMSCAN

**Table B –** Standards used for EPMA and lower limits of detection (LLD)

**Table C** – Standards used for LA-ICP-MS and detection limits.

**Table D** – Full EPMA sulphide data analysed by WDS. Standard information available in Table B.

976 **Table E** – Full LA-ICP-MS data for all sulphides analysed in this study. Note that '–' denotes ''isotope
977 not measured"; * Denotes isotopes which have been interference-corrected (Standard 1, Cardiff
978 University, matrix matched) for argide species and Cd; ** Se concentration based on $^{82}$Se isotope for
979 these samples (as opposed to $^{77}$Se for all others). Values in *italic font* indicate those below detection
980 limit, but stated as 50% detection limit to allow for plotting. Standard information available in Table
981 C.

982 **Figure A –** Silicate mineral chemistry. Ternary diagrams for sample RV-IM-15. (a) end-member
983 compositions of garnet (Pyp pyropem, GRS grossular, Alm almandine). (b) end-member compositions
984 of primary omphacitic clinopyroxenes (red), secondary Al-diopside (blue) and comparison to Roberts
985 Victor eclogite xenolith clinopyroxenes from Huang et al. (2012) (green) (Jd jadite, Aeg aegerine).

986 **Figure B –** All QEMSCAN field scans of BMS. (a) RV-IM-15 C Irregular BMS interstitial to garnet and
987 pervasive Al-diopside. The mss (pyrite/pyrrhotite) core can be clearly seen, as well as pentlandite
988 forming along internal fractures and forming an inner rim, chalcopyrite is forming the blocky outer
989 rim. (b) RV-IM-15 G Highly deteriorated BMS interstitial to clinopyroxenes and an albite vein. This BMS
990 lacks a distinct mss core and is solely composed of pentlandite and chalcopyrite. (c) RV-IM-15 E
991 Rounded BMS embayment in garnet. The fracture it sits within is predominantly secondary
992 clinopyroxene and biotite. The BMS has a mss core with pentlandite forming as internal fractures and
993 flames. In this BMS, pentlandite forms the dominant outer phase, with only minor chalcopyrite. (d)
994 RV-IM-18 D Rounded BMS semi-enclosed within the rim of a garnet. The BMS is within a fracture
995 within garnet, primarily infilled with chlorite. (e) RV-IM-18 C Rounded BMS enclosed within the same
996 garnet as (d), but located slightly further away from the rim. Mostly mss with minor blocky pentlandite
997 and chalcopyrite rim. Within the garnet there are inclusions and fractures containing chlorite, albite
998 and biotite.

999 **Figure C –** Time resolved analysis (TRA) plots of a selection of BMS analysed by LA-ICP-MS**.** TRA
1000 includes switch-off of the laser (white area after 'sample') and gas blank at the end of the analysis
1001 (grey area on the right hand side of each plot). Area of sample analysis (labelled 'sample' and

1002 interpolated for processing of LA-ICP-MS data) is delineated. (a) RV-IM-17 BMS1 and (b) RV-IM-01
1003 BMS1B. Both sets of TRA show mixed sulphides, zoned in Cu (such that RV-IM-17 BMS1 demonstrates
1004 classic texture of chalcopyrite at the rim of the BMS grain and mss in the centre). RV-IM-01 BMS1B
1005 shows more complex zonation of end-member sulphides with enrichment in Zn in the centre. Zonation
1006 in As and Ag appear in both TRA sets. PGE are present in higher concentrations in RV-IM-01 BMS1B
1007 and particularly this TRA set demonstrates PGM (probably as nano-nuggets) at the rims of the BMS
1008 grain.
1009 **Figure D –** Further bivariate plots of LA-ICP-MS data from BMS. Data are plotted according to sample
1010 number only. Corresponding data table is available in Table E of this supplementary dataset.
1011 **Figure E –** SEM BSE images of Ni-arsenide and PGM.
1012 **Figure F –** Trace element modelling of batch partial melting of Roberts Victor eclogite BMS. The top
1013 four panels show the concentration (chondrite normalised using the values of Fischer-Gödde et al.,
1014 2010) of Ni, PGE, Au, Re and Cu in the silicate melt generated at different degrees of partial melting
1015 of the BMS in the source (where F = melt fraction), according to different starting compositions. Each
1016 panel (top four models) use a starting composition from each of the four end-member BMS
1017 compositions identified in the Roberts Victor xenoliths analysed in this study (see Section 4.1). Note
1018 that due to the highly chalcophile behaviour of the PGE, > 99% of BMS (F = 0.999) must be extracted
1019 used from the source in order for the silicate melt to have a composition similar to the Bushveld
1020 parental magma compositions (B1-3 and UM). These top four models (shades of purple lines) were
1021 conducted assuming 0.5% (by volume) BMS in the source. The bottom panel of this figure (shades of
1022 red lines) shows modelling to demonstrate the effect of complete melting and extraction of the mean
1023 BMS composition of the Roberts Victor eclogite xenoliths (this study) but at different abundances of
1024 BMS in the mantle source (0.03 to 1 % BMS by volume). In summary, a higher abundance of BMS in
1025 the source leads to a higher concentration of chalcophile elements in the resulting silicate melt. Note
1026 that the mean Roberts Victor eclogitic BMS composition was calculated excluding the rare high-PGE
1027 BMS from RV-IM-02**.**

**References**


Ahmed, A.H., Arai, S. and Ikenne, M., 2009. Mineralogy and paragenesis of the Co-Ni arsenide ores of Bou Azzer, Anti-Atlas, Morocco. Economic Geology, 104(2), pp.249-266.

Alard O., Griffin W. L., Lorand, J.-P., E., Jackson S.E., O'Reilly S. Y., 2000. Non-chondritic distribution of the highly siderophile elements in mantle sulphides. Nature, 407, pp. 891–894.

Alard, O., Luguet, A., Pearson, N.J., Griffin, W.L., Lorand, J.P., Gannoun, A., Burton, K.W. and O'Reilly, S.Y., 2005. In situ Os isotopes in abyssal peridotites bridge the isotopic gap between MORBs and their source mantle. Nature, 436(7053), pp.1005-1008.

Alard, O., Lorand, J.P., Reisberg, L., Bodinier, J.L., Dautria, J.M., O'reilly, S.Y., 2011. Volatile-rich metasomatism in montferrier xenoliths (Southern France): Implications for the abundances of chalcophile and highly siderophile elements in the subcontinental mantle. Journal of Petrology, 52, pp. 2009–2045.

Aulbach, S., Creaser, R.A., Pearson, N.J., Simonetti, S.S., Heaman, L.M., Griffin, W.L., Stachel, T., 2009. Sulfide and whole rock Re-Os systematics of eclogite and pyroxenite xenoliths from the Slave Craton, Canada. Earth and Planetary Science Letters, 283, pp. 48–58.

Aulbach, S., Stachel, T., Heaman, L.M., Creaser, R.A. and Shirey, S.B., 2010. Formation of cratonic subcontinental lithospheric mantle from hybrid plume sources. Geochimica et Cosmochimica Acta, 74(12, Supplement), pp. A37-A37.

Aulbach, S., Stachel, T., Heaman, L.M., Creaser, R.A. and Shirey, S.B., 2011. Formation of cratonic subcontinental lithospheric mantle and complementary komatiite from hybrid plume sources. Contributions to Mineralogy and Petrology, 161(6), pp.947-960.

Aulbach, S., Stachel, T., Seitz, H.M., Brey, G.P., 2012. Chalcophile and siderophlie elements in sulphide inclusions in eclogitic diamonds and metal cycling in a Paleoproterozoic subduction zone. Geochimica et Cosmochimica Acta, 93, pp. 278-299.

Aulbach, S., Jacob, D.E., 2016. Major- and trace-elements in cratonic mantle eclogites and pyroxenites reveal heterogeneous sources and metamorphic processing of low-pressure protoliths. Lithos, 262, pp. 586–605.

Aulbach, S., Mungall, J.E., Pearson, D.G., 2016. Distribution and processing of highly siderophile elements in cratonic mantle lithosphere. Reviews in Mineralogy and Geochemistry 81 (1), pp. 239–304.

Aulbach, S., Jacob, D.E., Cartigny, P., Stern, R.A., Simonetti, S.S., Wörner, G., Viljoen, K.S., 2017. Eclogite xenoliths from Orapa: Ocean crust recycling, mantle metasomatism and carbon cycling at the western Zimbabwe craton margin. Geochimica et Cosmochimica Acta 213, pp. 574–592.

Barnes, S.J., Maier, W.D. and Curl, E.A., 2010. Composition of the marginal rocks and sills of the Rustenburg Layered Suite, Bushveld Complex, South Africa: implications for the formation of the platinum-group element deposits. Economic Geology, 105(8), pp.1491-1511.

Barnes, S.J., Mungall, J.E., Maier, W.D., 2015. Platinum group elements in mantle melts and mantle samples. Lithos, 232: 395-417.

Becker, H., Horan, M.F., Walker, R.J., Gao, S., Lorand, J.P. and Rudnick, R.L., 2006. Highly siderophile element composition of the Earth's primitive upper mantle: constraints

from new data on peridotite massifs and xenoliths. Geochimica et Cosmochimica Acta, 70(17), pp.4528-4550.
Bockrath, C., Ballhaus, C. and Holzheid, A., 2004. Fractionation of the platinum-group elements during mantle melting. Science, 305(5692), pp.1951-1953.
Brenan, J.M., 2015. Se–Te fractionation by sulfide–silicate melt partitioning: implications for the composition of mantle-derived magmas and their melting residues. Earth and Planetary Science Letters, 422, pp.45-57.
Brenan, J.M. and Andrews, D., 2001. High-temperature stability of laurite and Ru–Os–Ir alloy and their role in PGE fractionation in mafic magmas. The Canadian Mineralogist, 39(2), pp.341-360.
Brey, G.P., Shu, Q., 2018. The birth, growth and ageing of the Kaapvaal subcratonic mantle. Mineralogy and Petrology, 112, pp. 23–41.
Bulanova, G.P., Griffin, W.L., Ryan, C.G., Shestakova, O.Y., Barnes, S.J., 1996. Trace elements in sulfide inclusions from Yakutian diamonds. Contributions to Mineralogy and Petrology, 124(2), pp. 111-125.
Burness, S., Smart, K.A., Tappe, S., Stevens, G., Woodland, A.B., Cano, E., 2020. Sulphur-rich mantle metasomatism of Kaapvaal craton eclogites and its role in redox-controlled platinum group element mobility. Chemical Geology, 542.
Choi, E., Fiorentini, M.L., Hughes, H.S. and Giuliani, A., 2020. Platinum-group element and Au geochemistry of Late Archean to Proterozoic calc-alkaline and alkaline magmas in the Yilgarn Craton, Western Australia. Lithos, 374, p.105716.
Coggon, J.A., Nowell, G.M., Pearson, D.G., Oberthür, T., Lorand, J.P., Melcher, F. and Parman, S.W., 2012. The 190Pt–186Os decay system applied to dating platinum-group element mineralization of the Bushveld Complex, South Africa. Chemical Geology, 302, pp.48-60.
Dale, C.W., Burton, K.W., Pearson, D.G., Gannoun, A., Alard, O., Argles, T.W. and Parkinson, I.J., 2009. Highly siderophile element behaviour accompanying subduction of oceanic crust: whole rock and mineral-scale insights from a high-pressure terrain. Geochimica et Cosmochimica Acta, 73(5), pp.1394-1416.
De Wit, M.J., De Ronde, C.E.J., Tredoux, M., Roering, C., Hart, R.J., Armstrong, R.A., Green, R.W.E., Peberdy, E., Hart, R.A., 1992. Formation of an Archaean continent. Nature, 357, pp. 553–562.
Deines, P., Harris, J.W., 1995. Sulfide inclusion chemistry and carbon isotopes of African diamonds. Geochimica et Cosmochimica Acta, 59, pp. 3173-3188.
Delpech, G., Lorand, J.-P., Grégoire,M., Cottin, J.-Y.,O'Reilly, S.Y., 2012. In-situ geochemistry of sulfides in highly metasomatized mantle xenoliths from Kerguelen, southern Indian Ocean. Lithos, 154, pp. 296–314.
Dreibus, G., Palme, H., Spettel, B., Zipfel, J. and Wänke, H., 1995. Sulfur and selenium in chondritic meteorites. Meteoritics, 30(4), pp.439-445.
Eggler, D.H., Lorand, J.P., 1993.Mantle sulfide geobarometry. Geochimica et Cosmochimica Acta, 57 (10), 2213–2222.
Eriksson, P.G., Rigby, M.J., Bandopadhyay, P.C., Steenkamp, N.C., 2011. The Kaapvaal Craton, South Africa: no evidence for a supercontinental affinity prior to 2.0 Ga? International Geology Review, 53, pp. 1312–1330.
Ferraris, C., Lorand, J.-P., 2014. Novodneprite (AuPb3), anyuiite [Au(Pb, Sb)2] and gold micro- and nano-inclusions within plastically deformed mantle-derived olivine from

the Lherz peridotite (Pyrenees, France): a HRTEM–AEM–EELS study. Physics and Chemistry of Minerals, 42 (2), 143–150.
Field, M., Stiefenhofer, J., Robey, J. and Kurszlaukis, S., 2008. Kimberlite-hosted diamond deposits of southern Africa: a review. Ore Geology Reviews, 34(1-2), pp.33-75.
Fischer-Gödde, M., Becker, H. and Wombacher, F., 2010. Rhodium, gold and other highly siderophile element abundances in chondritic meteorites. Geochimica et Cosmochimica Acta, 74(1), pp.356-379.
Fung, A.T., Haggerty, S.E., 1995. Petrography and mineral compositions of eclogites from the Koidu kimberlite complex, Sierra-Leone. Journal of Geophysical Research-Solid Earth, 100(B10), pp. 20451-20473.
Good, N., De Wit, M.J., 1997. The Thabazimbi-Murchison lineament of the Kaapvaal Craton, South Africa: 2700 Ma of episodic deformation. Journal of the Geological Society, 154, pp. 93–97.
Goodall, W.R. and Scales, P.J., 2007. An overview of the advantages and disadvantages of the determination of gold mineralogy by automated mineralogy. Minerals Engineering, 20(5), pp.506-517.
Goodall, W.R., Scales, P.J. and Butcher, A.R., 2005. The use of QEMSCAN and diagnostic leaching in the characterisation of visible gold in complex ores. Minerals Engineering, 18(8), pp.877-886.
Gottlieb, P., Wilkie, G., Sutherland, D., Ho-Tun, E., Suthers, S., Perera, K., Jenkins, B., Spencer, S., Butcher, A. and Rayner, J., 2000. Using quantitative electron microscopy for process mineralogy applications. The Journal of the Minerals, Metals and Materials Society, 52, pp.24–25.
Gréau, Y., 2011. Siderophile and chalcophile elements in Roberts Victor eclogites: insights on the generation of mantle heterogeneity (Doctoral dissertation, Macquarie University).
Gréau, Y., Alard, O., Griffin, W.L., Huang, J.X., O'Reilly, S.Y., 2013. Sulfides and chalcophile elements in Roberts Victor eclogites: Unravelling a sulfide-rich metasomatic event. Chemical Geology.
Gréau, Y., Griffin, W.L., Alard, O. and O'Reilly, S.Y., 2008, October. Petrology and geochemistry of eclogitic sulphides: a new insight on origin of mantle eclogites?. In International Kimberlite Conference: Extended Abstracts, 9.
Green, D.H., Hibberson, W.O., Kovacs, I., Rosenthal, A., 2010. Water and its influence on the lithosphere-asthenosphere boundary. Nature, 467(7314), pp. 448-451.
Griffin, W.L., O'Reilly, S.Y., 2007. Cratonic lithospheric mantle: Is anything subducted?, in: Episodes, pp. 43–53.
Griffin, W.L., O'Reilly, S.Y., Abe, N., Aulbach, S., Davies, R.M., Pearson, N.J., Doyle, B.J., Kivi, K., 2003a. The origin and evolution of Archean lithospheric mantle. Precambrian Research, 127, pp. 19–41.
Griffin, W.L., O'Reilly, S.Y., Natapov, L.M., Ryan, C.G., 2003b. The evolution of lithospheric mantle beneath the Kalahari Craton and its margins. Lithos, 71: 215–241.
Gurney, J.J. and Kirkley, M.B., 1996. Kimberlite dyke mining in South Africa. Africa Geoscience Review, 3(2), pp. 191-201.
Harris, C., Pronost, J.J., Ashwal, L.D. and Cawthorn, R.G., 2005. Oxygen and hydrogen isotope stratigraphy of the Rustenburg Layered Suite, Bushveld Complex: constraints on crustal contamination. Journal of Petrology, 46(3), pp.579-601.

Hart, S.R. and Kinloch, E.D., 1989. Osmium isotope systematics in Witwatersrand and Bushveld ore deposits. Economic Geology, 84(6), pp.1651-1655.

Harte, B. and Gurney, J.J., 1975. Evolution of clinopyroxene and garnet in an eclogite nodule from the Roberts Victor kimberlite pipe, South Africa. In Physics and Chemistry of the Earth, pp. 367-387. Pergamon.

Harvey, J., König, S. and Luguet, A., 2015. The effects of melt depletion and metasomatism on highly siderophile and strongly chalcophile elements: S–Se–Te–Re–PGE systematics of peridotite xenoliths from Kilbourne Hole, New Mexico. Geochimica et Cosmochimica Acta, 166, pp.210-233.

Hatton, C.J., 1995. Mantle plume origin for the Bushveld and Ventersdorp magmatic provinces. Journal of African Earth Sciences, 21(4), pp.571-577.

Hatton, C.J. and Gurney, J.J., 1977, September. A diamond graphite eclogite from the Roberts Victor Mine. In International Kimberlite Conference: Extended Abstracts, 2, pp. 141-143.

Heaman, L.M., Creaser, R.A., Cookenboo, H.O., Chacko, T., 2006. Multi-stage modification of the northern Slave mantle lithosphere: evidence from zircon- and diamond-bearing eclogite xenoliths entrained in Jericho kimberlite, Canada. Journal of Petrology, 47(4), pp. 821-858.

Helmy, H.M., Ballhaus, C., Berndt, J., Bockrath, C., Wohlgemuth-Ueberwasser, C., 2007. Formation of Pt, Pd and Ni tellurides: experiments in sulfide-telluride systems. Contributions to Mineralogy and Petrology, 153, pp. 577–591.

Herzberg, C., Zhang, J.Z., 1996. Melting experiments on anhydrous peridotite KLB-1: Compositions of magmas in the upper mantle and transition zone. Journal of Geophysical Research-Solid Earth, 101(B4), pp. 8271-8295.

Hills, D.V., Haggerty, S.E., 1989. Petrochemistry of eclogites from the Koidu kimberlite complex, Sierra-Leone. Contributions to Mineralogy and Petrology, 103(4), pp. 397-422.

Holwell, D.A., McDonald, I., 2010. A review of the behaviour of platinum group elements within natural magmatic sulfide ore systems. Platinum Metals Review, 54, pp. 26–36.

Holwell, D.A., Adeyemi, Z., Ward, L.A., Smith, D.J., Graham, S.D., McDonald, I. and Smith, J.W., 2017. Low temperature alteration of magmatic Ni-Cu-PGE sulfides as a source for hydrothermal Ni and PGE ores: A quantitative approach using automated mineralogy. Ore Geology Reviews, 91, pp.718-740.

Holwell, D.A., Fiorentini, M., McDonald, I., Lu, Y., Giuliani, A., Smith, D.J., Keith, M. and Locmelis, M., 2019. A metasomatized lithospheric mantle control on the metallogenic signature of post-subduction magmatism. Nature communications, 10(1), pp.1-10.

Huang, J.X., Gréau, Y., Griffin, W.L., O'Reilly, S.Y. and Pearson, N.J., 2012. Multi-stage origin of Roberts Victor eclogites: progressive metasomatism and its isotopic effects. Lithos, 142, pp.161-181.

Huang, J.X., Li, P., Griffin, W.L., Xia, Q.K., Gréau, Y., Pearson, N.J. and O'Reilly, S.Y., 2014. Water contents of Roberts Victor xenolithic eclogites: primary and metasomatic controls. Contributions to Mineralogy and Petrology, 168(6), p.1092.

Hughes, H.S., McDonald, I. and Kerr, A.C., 2015. Platinum-group element signatures in the North Atlantic Igneous Province: implications for mantle controls on metal budgets during continental breakup. Lithos, 233, pp.89-110.

1212 Hughes, H.S., McDonald, I., Loocke, M., Butler, I.B., Upton, B.G. and Faithfull, J.W., 2017.
1213 Paradoxical co-existing base metal sulphides in the mantle: the multi-event record
1214 preserved in Loch Roag peridotite xenoliths, North Atlantic Craton. Lithos, 276,
1215 pp.103-121.
1216 Jacob, D.E., 2004. Nature and origin of eclogite xenoliths from kimberlites. Lithos, 77(1-4),
1217 pp. 295-316.
1218 James, D.E., Boyd, F.R., Schutt, D., Bell, D.R., Carlson, R.W., 2004. Xenolith constraints on
1219 seismic velocities in the upper mantle beneath southern Africa. Geochemistry
1220 Geophysics Geosystems, 5.
1221 Jacob, D.E., Schmickler, B. and Schulze, D.J., 2003. Trace element geochemistry of coesite-
1222 bearing eclogites from the Roberts Victor kimberlite, Kaapvaal craton. Lithos, 71(2-
1223 4), pp.337-351.
1224 Jacob, D.E., Bizimis, M. and Salters, V.J.M., 2005. Lu–Hf and geochemical systematics of
1225 recycled ancient oceanic crust: evidence from Roberts Victor eclogites. Contributions
1226 to Mineralogy and Petrology, 148(6), pp.707-720.
1227 Jelsma, H., Barnett, W., Richards, S., Lister, G., 2009. Tectonic setting of kimberlites. Lithos,
1228 112, pp. 155–165.
1229 Kiseeva, E.S., Fonseca, R.O.C., Smythe, D.J., 2017a. Chalcophile elements and sulfides in the
1230 upper mantle. Elements, 13(2), pp. 111-116.
1231 Kiseeva, E.S., Kamenetsky, V.S., Yaxley, G.M., Shee, S.R., 2017b. Mantle melting versus
1232 mantle metasomatism - "The chicken or the egg" dilemma. Chemical Geology, 455,
1233 pp. 120-130.
1234 König, S., Luguet, A., Lorand, J.P., Wombacher, F. and Lissner, M., 2012. Selenium and
1235 tellurium systematics of the Earth's mantle from high precision analyses of ultra-
1236 depleted orogenic peridotites. Geochimica et Cosmochimica Acta, 86, pp.354-366.
1237 Kramers, J.D., 1979. Lead, uranium, strontium, potassium and rubidium in inclusion-bearing
1238 diamonds and mantle-derived xenoliths from southern Africa. Earth and Planetary
1239 Science Letters, 42(1), pp.58-70.
1240 Krogh, E.J., 1988. The garnet–clinopyroxene Fe\Mg geothermometer—a reinterpretation of
1241 existing experimental data. Contributions to Mineralogy and Petrology, 99, pp. 44–
1242 48.
1243 Locmelis, M., Fiorentini, M.L., Barnes, S.J. and Pearson, N.J., 2013. Ruthenium variation in
1244 chromite from komatiites and komatiitic basalts—a potential mineralogical indicator
1245 for nickel sulfide mineralization. Economic Geology, 108(2), pp.355-364.
1246 Lorand, J.-P., Alard, O., 2010. Determination of selenium and tellurium concentrations in
1247 Pyrenean peridotites (Ariege, France): new insight into S/Se/Te systematics of the
1248 upper in mantle samples. Chemical Geology 278, pp. 120–130.
1249 Lorand, J.P., Alard, O., Luguet, A., Keays, R.R., 2003. Sulfur and selenium systematics of the
1250 subcontinental lithospheric mantle: Inferences from the Massif Central xenolith suite
1251 (France). Geochimica et Cosmochimica Acta.
1252 Lorand, J.-P., Grégoire, M., 2006. Petrogenesis of basemetal sulphide assemblages of some
1253 peridotites from the Kaapvaal craton (South Africa). Contributions toMineralogy and
1254 Petrology 151 (5), pp. 521–538.
1255 Lorand, J.P. and Luguet, A., 2016. Chalcophile and siderophile elements in mantle rocks:
1256 Trace elements controlled by trace minerals. Reviews in Mineralogy and
1257 Geochemistry, 81(1), pp.441-488.

Lorand, J.P., Alard, O. and Luguet, A., 2010. Platinum-group element micronuggets and refertilization process in Lherz orogenic peridotite (northeastern Pyrenees, France). Earth and Planetary Science Letters, 289(1-2), pp.298-310.

Lorand, J.P., Luguet, A. and Alard, O., 2013. Platinum-group element systematics and petrogenetic processing of the continental upper mantle: A review. Lithos, 164, pp.2-21.

Luguet, A. and Reisberg, L., 2016. Highly siderophile element and 187Os signatures in non-cratonic basalt-hosted peridotite xenoliths: Unravelling the origin and evolution of the post-Archean lithospheric mantle. Reviews in Mineralogy and Geochemistry, 81(1), pp.305-367.

MacGregor, I.D. and Manton, W.I., 1986. Roberts Victor eclogites: ancient oceanic crust. Journal of Geophysical Research: Solid Earth, 91(B14), pp.14063-14079.

Manton, W.I. and Tatsumoto, M., 1971. Some Pb and Sr isotopic measurements on eclogites from the Roberts Victor mine, South Africa. Earth and Planetary Science Letters, 10(2), pp.217-226.

Macgregor, I.D. and Carter, J.L., 1970. The chemistry of clinopyroxenes and garnets of eclogite and peridotite xenoliths from the Roberts Victor mine, South Africa. Physics of the Earth and Planetary Interiors, 3, pp.391-397.

McCandless, T.E. and Ruiz, J., 1991. Osmium isotopes and crustal sources for platinum-group mineralization in the Bushveld Complex, South Africa. Geology, 19(12), pp.1225-1228.

McLean, H., Banas, A., Creighton, S., Whiteford, S., Luth, R.W. and Stachel, T., 2007. Garnet xenocrysts from the Diavik mine, NWT, Canada: Composition, color, and paragenesis. The Canadian Mineralogist, 45(5), pp.1131-1145.

McDonald, I. and Viljoen, K.S., 2006. Platinum-group element geochemistry of mantle eclogites: a reconnaissance study of xenoliths from the Orapa kimberlite, Botswana. Applied Earth Science, 115(3), pp.81-93.

McDonough, W.F. and Sun, S.S., 1995. The composition of the Earth. Chemical geology, 120(3-4), pp.223-253.

Miller, W.G., Holland, T.J. and Gibson, S.A., 2016. Garnet and spinel oxybarometers: new internally consistent multi-equilibria models with applications to the oxidation state of the lithospheric mantle. Journal of Petrology, 57(6), pp.1199-1222.

Moore, A., Blenkinsop, T., Cotterill, F., 2008. Controls on post-Gondwana alkaline volcanism in Southern Africa. Earth and Planetary Science Letters, 268, pp. 151–164.

Mungall, J.E. and Brenan, J.M., 2014. Partitioning of platinum-group elements and Au between sulfide liquid and basalt and the origins of mantle-crust fractionation of the chalcophile elements. Geochimica et Cosmochimica Acta, 125, pp.265-289.

Naldrett, A.J., 2011. Fundamentals of magmatic sulfide deposits. Reviews in Economic Geology, 17(1), pp. 1-50.

Ongley, J.S., Basu, A.R. and Kyser, T.K., 1987. Oxygen isotopes in coexisting garnets, clinopyroxenes and phlogopites of Roberts Victor eclogites: implications for petrogenesis and mantle metasomatism. Earth and Planetary Science Letters, 83(1-4), pp.80-84.

Patten, C., Barnes, S.J., Mathez, E.A. and Jenner, F.E., 2013. Partition coefficients of chalcophile elements between sulfide and silicate melts and the early crystallization history of sulfide liquid: LA-ICP-MS analysis of MORB sulfide droplets. Chemical Geology, 358, pp.170-188.

Pitcher, L., Helz, R.T., Walker, R.J. and Piccoli, P., 2009. Fractionation of the platinum-group elments and Re during crystallization of basalt in Kilauea Iki Lava Lake, Hawaii. Chemical Geology, 260(3-4), pp.196-210.

Prichard, H.M., Knight, R.D., Fisher, P.C., McDonald, I., Zhou, M.F. and Wang, C.Y., 2013. Distribution of platinum-group elements in magmatic and altered ores in the Jinchuan intrusion, China: an example of selenium remobilization by postmagmatic fluids. Mineralium Deposita, 48(6), pp.767-786.

Richardson S.H., Shirey S.B., 2008. Continental mantle signature of Bushveld magmas and coeval diamonds. Nature, 453, pp. 910–913.

Richardson S.H., Shirey S.B., Harris J.W., 2004. Episodic diamond genesis at Jwaneng, Botswana, and implications for Kaapvaal craton evolution. Lithos 77, pp. 143–154.

Rollinson, G.K., Andersen, J.C., Stickland, R.J., Boni, M. and Fairhurst, R., 2011. Characterisation of non-sulphide zinc deposits using QEMSCAN®. Minerals Engineering, 24(8), pp.778-787.

Saunders, J.E., Pearson, N.J., O'Reilly, S.Y., Griffin, W.L., 2015. Sulfide metasomatism and the mobility of gold in the lithospheric mantle. Chemical Geology, 410, pp. 149–161.

Sautter, V. and Harte, B., 1988. Diffusion gradients in an eclogite xenolith from the Roberts Victor kimberlite pipe: 1. Mechanism and evolution of garnet exsolution in Al2O3-rich clinopyroxene. Journal of Petrology, 29(6), pp.1325-1352.

Savelyev, D.P., Kamenetsky, V.S., Danyushevsky, L.V., Botcharnikov, R.E., Kamenetsky, M.B., Park, J.W., Portnyagin, M.V., Olin, P., Krasheninnikov, S.P., Hauff, F. and Zelenski, M.E., 2018. Immiscible sulfide melts in primitive oceanic magmas: Evidence and implications from picrite lavas (Eastern Kamchatka, Russia). American Mineralogist: Journal of Earth and Planetary Materials, 103(6), pp.886-898.

Schoenberg, R., Kruger, F.J., Nägler, T.F., Meisel, T. and Kramers, J.D., 1999. PGE enrichment in chromitite layers and the Merensky Reef of the western Bushveld Complex; a Re–Os and Rb–Sr isotope study. Earth and Planetary Science Letters, 172(1-2), pp.49-64.

Shu, Q., Brey, G.P., Gerdes, A. and Hoefer, H.E., 2013. Geochronological and geochemical constraints on the formation and evolution of the mantle underneath the Kaapvaal craton: Lu–Hf and Sm–Nd systematics of subcalcic garnets from highly depleted peridotites. Geochimica et Cosmochimica Acta, 113, pp.1-20.

Schulze, D.J., 1989. Constraints on the abundance of eclogite in the upper mantle. Journal of Geophysical Research-Solid Earth and Planets, 94(B4), pp, 4205-4212.

Schmitz, M.D., Bowring, S.A., de Wit, M.J., Gartz, V., 2004. Subduction and terrane collision stabilize the western Kaapvaal craton tectosphere 2.9 billion years ago. Earth and Planetary Science Letters, 222, pp. 363–376.

Shirey, S.B., Richardson, S.H., 2011. Start of the wilson cycle at 3 Ga shown by diamonds from subcontinental mantle. Science, 333, pp. 434–436.

Simon, N.S.C., Carlson, R.W., Pearson, D.G., Davies, G.R., 2007. The origin and evolution of the Kaapvaal Cratonic Lithospheric Mantle. Journal of Petrology, 48, pp. 589–625.

Smith, J.W., Holwell, D.A. and McDonald, I., 2014. Precious and base metal geochemistry and mineralogy of the Grasvally Norite–Pyroxenite–Anorthosite (GNPA) member, northern Bushveld Complex, South Africa: implications for a multistage emplacement. Mineralium Deposita, 49(6), pp.667-692.

Spandler, C., Yaxley, G., Green, D.H., Rosenthal, A., 2008. Phase relations and melting of anhydrous K-bearing eclogite from 1200 to 1600°C and 3 to 5 GPa. Journal of Petrology, 49(4), pp. 771-795.

Stachel, T., Harris, J.W., 2008. The origin of cratonic diamonds - Constraints from mineral inclusions. Ore Geology Reviews, 34(1-2), pp. 5-32.
Tappe, S., Smart, K., Torsvik, T., Massuyeau, M. and de Wit, M., 2018. Geodynamics of kimberlites on a cooling Earth: clues to plate tectonic evolution and deep volatile cycles. Earth and Planetary Science Letters, 484, pp.1-14.
Thomassot, E., Farquhar, J., Bouden, N., Harris, J.W., McKeegan, K., Cliff, J., Wing, B. and Piccoli, P., 2017, September. The Archean sedimentary sulfur recycling under the Kaapvaal craton revisited from 4S-isotopic compositions in sulfide inclusions in diamonds from Kimberley Pool (South Africa) Jwaneng and Orapa (Botswana). In International Kimberlite Conference: Extended Abstracts (Vol. 11).
Walker, R.J., Carlson, R.W., Shirey, S.B., F.R, B., 1989. Os, Sr, Nd, and Pb isotope systematics of southern African peridotite xenoliths: Implications for the chemical evolution of subcontinental mantle. Geochimica et Cosmochimica Acta, 53, pp. 1583–1595.
Willmore, C.C., Boudreau, A.E., Spivack, A. and Kruger, F.J., 2002. Halogens of Bushveld Complex, South Africa: δ37Cl and Cl/F evidence for hydration melting of the source region in a back-arc setting. Chemical Geology, 182(2-4), pp.503-511.
Wilson, A.H., Zeh, A. and Gerdes, A., 2017. In situ Sr isotopes in plagioclase and trace element systematics in the lowest part of the Eastern Bushveld Complex: dynamic processes in an evolving magma chamber. Journal of Petrology, 58(2), pp.327-360.
Yaxley, G.M., Brey, G.P., 2004. Phase relations of carbonate-bearing eclogite assemblages from 2.5 to 5.5 GPa: implications for petrogenesis of carbonatites. Contributions to Mineralogy and Petrology, 146(5), pp. 606-619.
Zeh, A., Ovtcharova, M., Wilson, A.H., Schaltegger, U., 2015. The Bushveld Complex was emplaced and cooled in less than one million years - results of zirconology, and geotectonic implications. Earth and Planetary Science Letters.
Zeh, A., Wilson, A.H., Gudelius, D., Gerdes, A., 2020. Hafnium Isotopic Composition of the Bushveld Complex Requires Mantle Melt–Upper Crust Mixing: New Evidence from Zirconology of Mafic, Felsic and Metasedimentary Rocks. Journal of Petrology, 40, pp. 550–32.
Zhang, Z., Lentsch, N. and Hirschmann, M.M., 2015. Carbon-saturated monosulfide melting in the shallow mantle: solubility and effect on solidus. Contributions to Mineralogy and Petrology, 170(5-6), p.47.
Zirakparvar, N.A., Mathez, E.A., Scoates, J.S. and Wall, C.J., 2014. Zircon Hf isotope evidence for an enriched mantle source for the Bushveld Igneous Complex. Contributions to Mineralogy and Petrology, 168(3), p.1050.
Zirakparvar, N.A., Mathez, E.A., Rajesh, H.M., Choe, S., 2019. Lu-Hf isotopic evidence of a deep mantle plume source for the ~2.06 Ga Bushveld Large Igneous Province. Lithos, 348-349, pp. 105-168.

Fig. 1

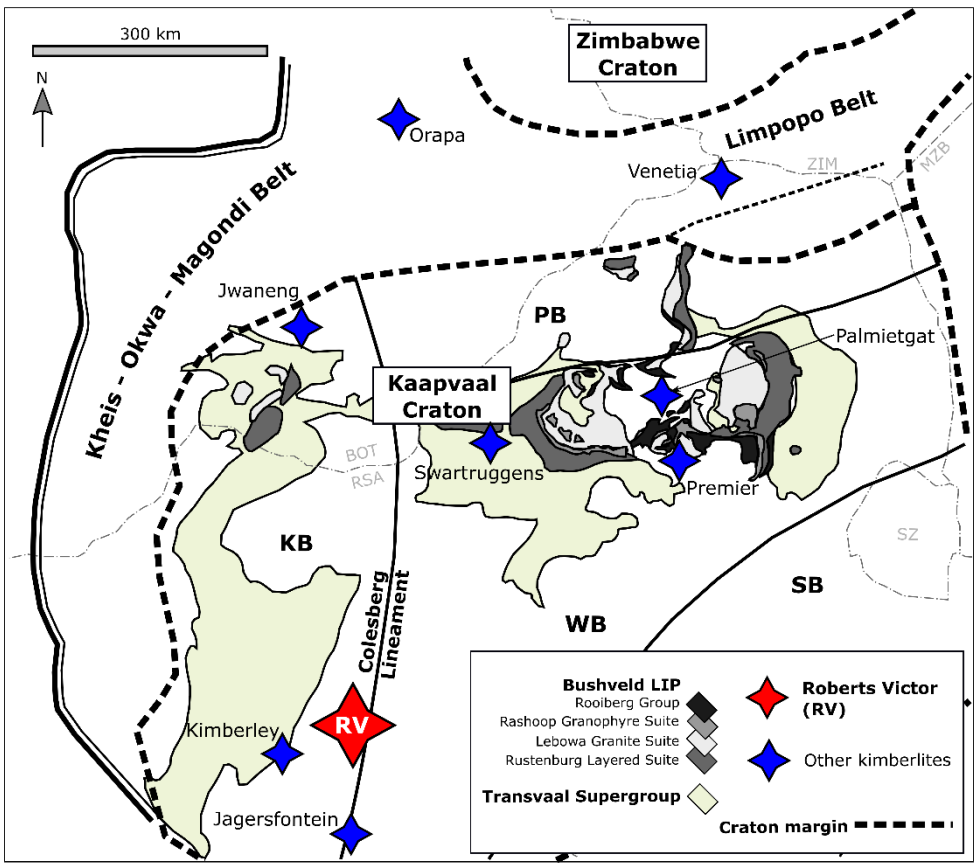
300 km
N
Zimbabwe Craton
Orapa
Limpopo Belt
Venetia
ZIM
MZB
Kheis - Okwa - Magondi Belt
Jwaneng
PB
Palmietgat
Kaapvaal Craton
BOT
RSA
Swartruggens
Premier
SZ
KB
SB
WB
Colesberg Lineament
Kimberley
RV
Jagersfontein
Bushveld LIP
Rooiberg Group
Rashoop Granophyre Suite
Lebowa Granite Suite
Rustenburg Layered Suite
Transvaal Supergroup
Roberts Victor (RV)
Other kimberlites
Craton margin

Fig. 2

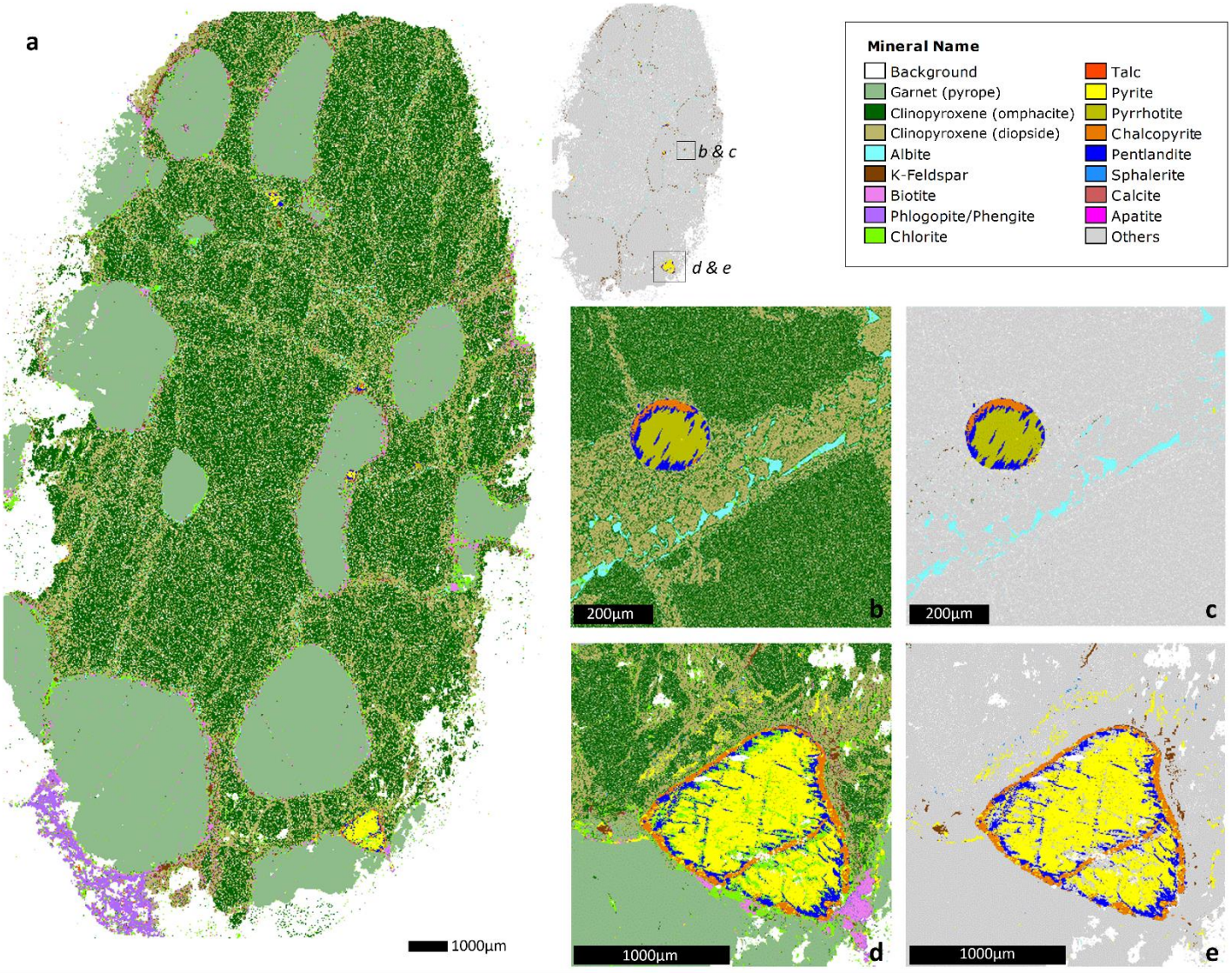
a
b & c
d & e
Mineral Name
Background
Garnet (pyrope)
Clinopyroxene (omphacite)
Clinopyroxene (diopside)
Albite
K-Feldspar
Biotite
Phlogopite/Phengite
Chlorite
Talc
Pyrite
Pyrrhotite
Chalcopyrite
Pentlandite
Sphalerite
Calcite
Apatite
Others
1000µm
200µm
b
200µm
c
1000µm
d
1000µm
e

Fig. 3

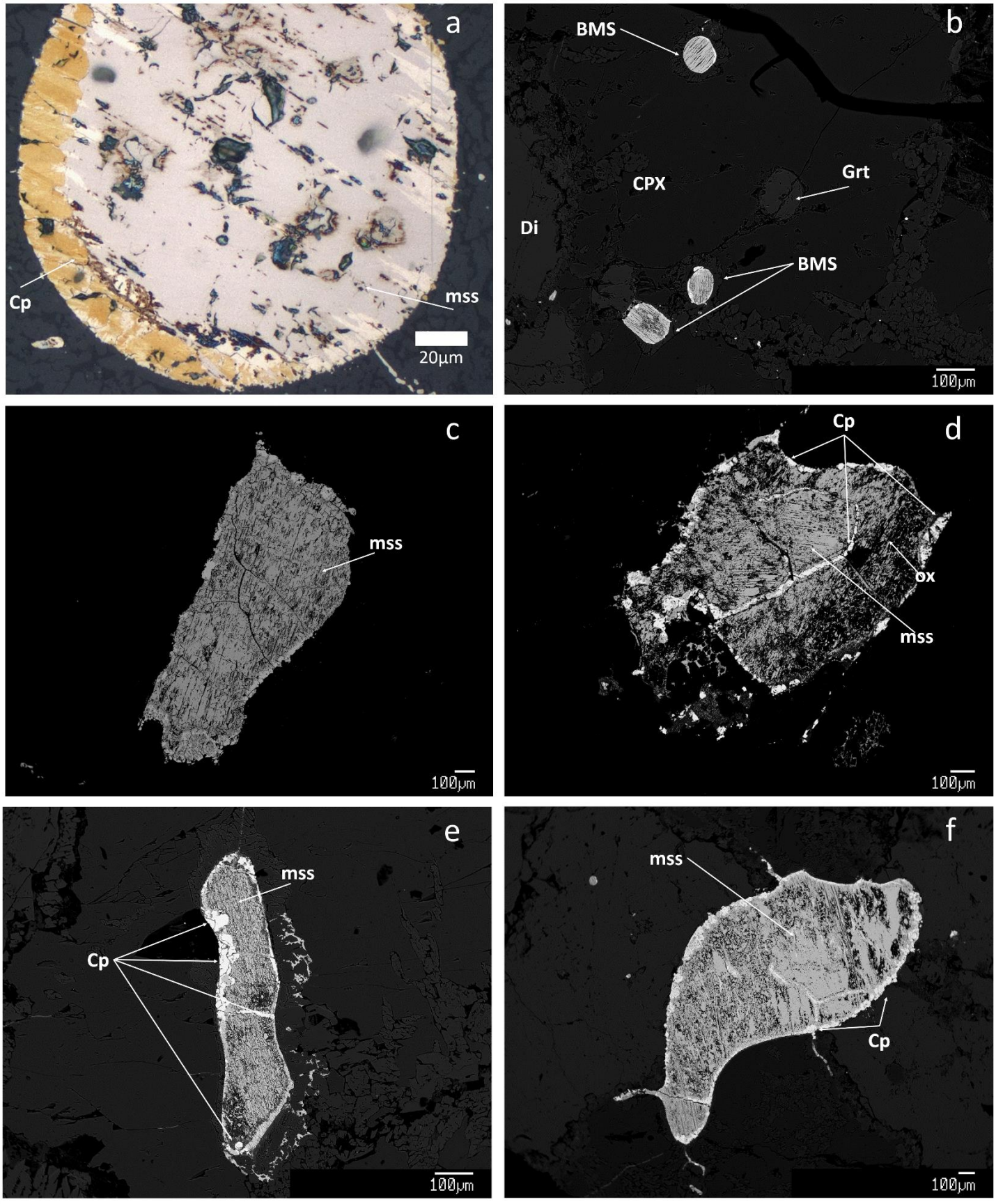
a
Cp
mss
20µm
b
BMS
CPX
Grt
Di
BMS
100µm
c
mss
100µm
d
Cp
ox
mss
100µm
e
mss
Cp
100µm
f
mss
Cp
100µm

Fig. 4

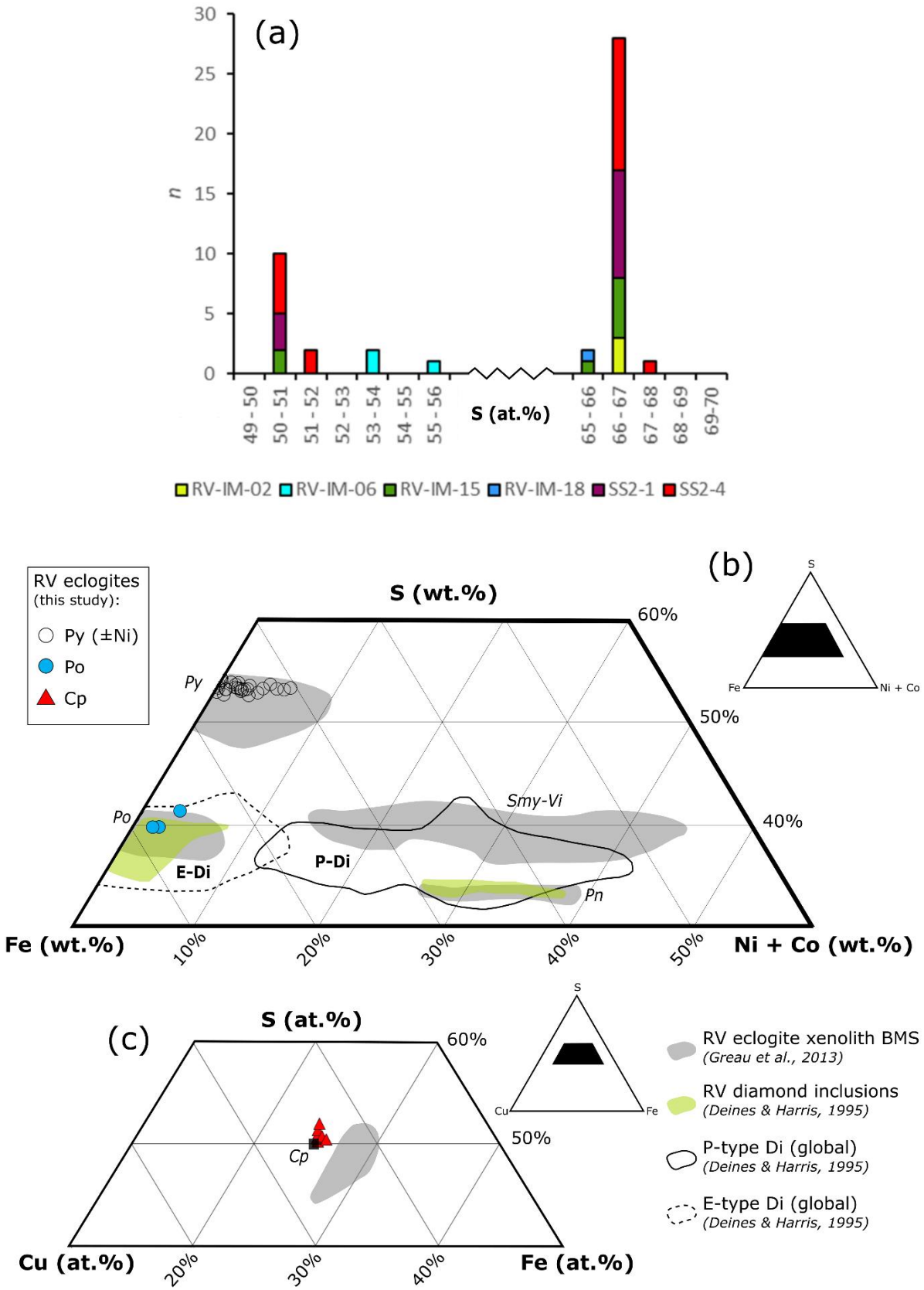
(a)
n
S (at.%)
49 - 50
50 - 51
51 - 52
52 - 53
53 - 54
54 - 55
55 - 56
65 - 66
66 - 67
67 - 68
68 - 69
69-70
RV-IM-02
RV-IM-06
RV-IM-15
RV-IM-18
SS2-1
SS2-4
RV eclogites
(this study):
Py (±Ni)
Po
Cp
(b)
S (wt.%)
Fe (wt.%)
Ni + Co (wt.%)
Py
Po
E-Di
P-Di
Smy-Vi
Pn
(c)
S (at.%)
Cu (at.%)
Fe (at.%)
Cp
RV eclogite xenolith BMS
(Greau et al., 2013)
RV diamond inclusions
(Deines & Harris, 1995)
P-type Di (global)
(Deines & Harris, 1995)
E-type Di (global)
(Deines & Harris, 1995)

Fig. 5

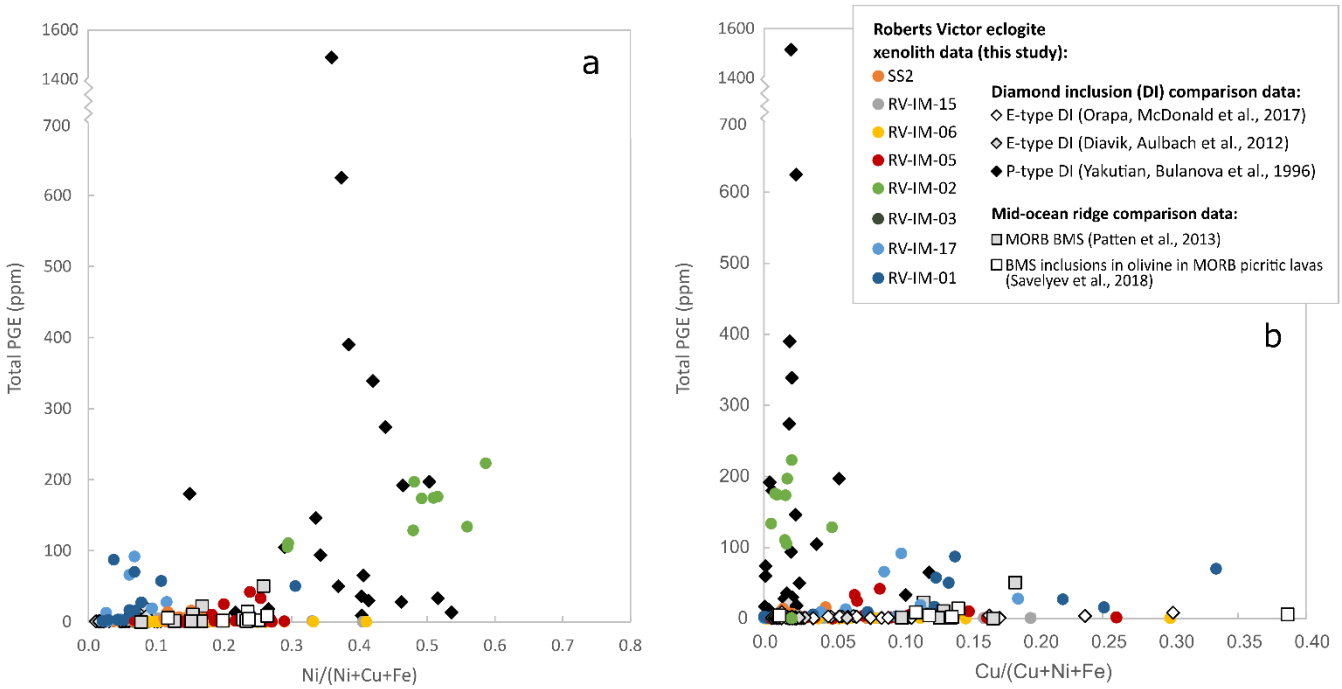
a
b
Total PGE (ppm)
Ni/(Ni+Cu+Fe)
Cu/(Cu+Ni+Fe)
Roberts Victor eclogite xenolith data (this study):
SS2
RV-IM-15
RV-IM-06
RV-IM-05
RV-IM-02
RV-IM-03
RV-IM-17
RV-IM-01
Diamond inclusion (DI) comparison data:
E-type DI (Orapa, McDonald et al., 2017)
E-type DI (Diavik, Aulbach et al., 2012)
P-type DI (Yakutian, Bulanova et al., 1996)
Mid-ocean ridge comparison data:
MORB BMS (Patten et al., 2013)
BMS inclusions in olivine in MORB picritic lavas (Savelyev et al., 2018)

Fig.6

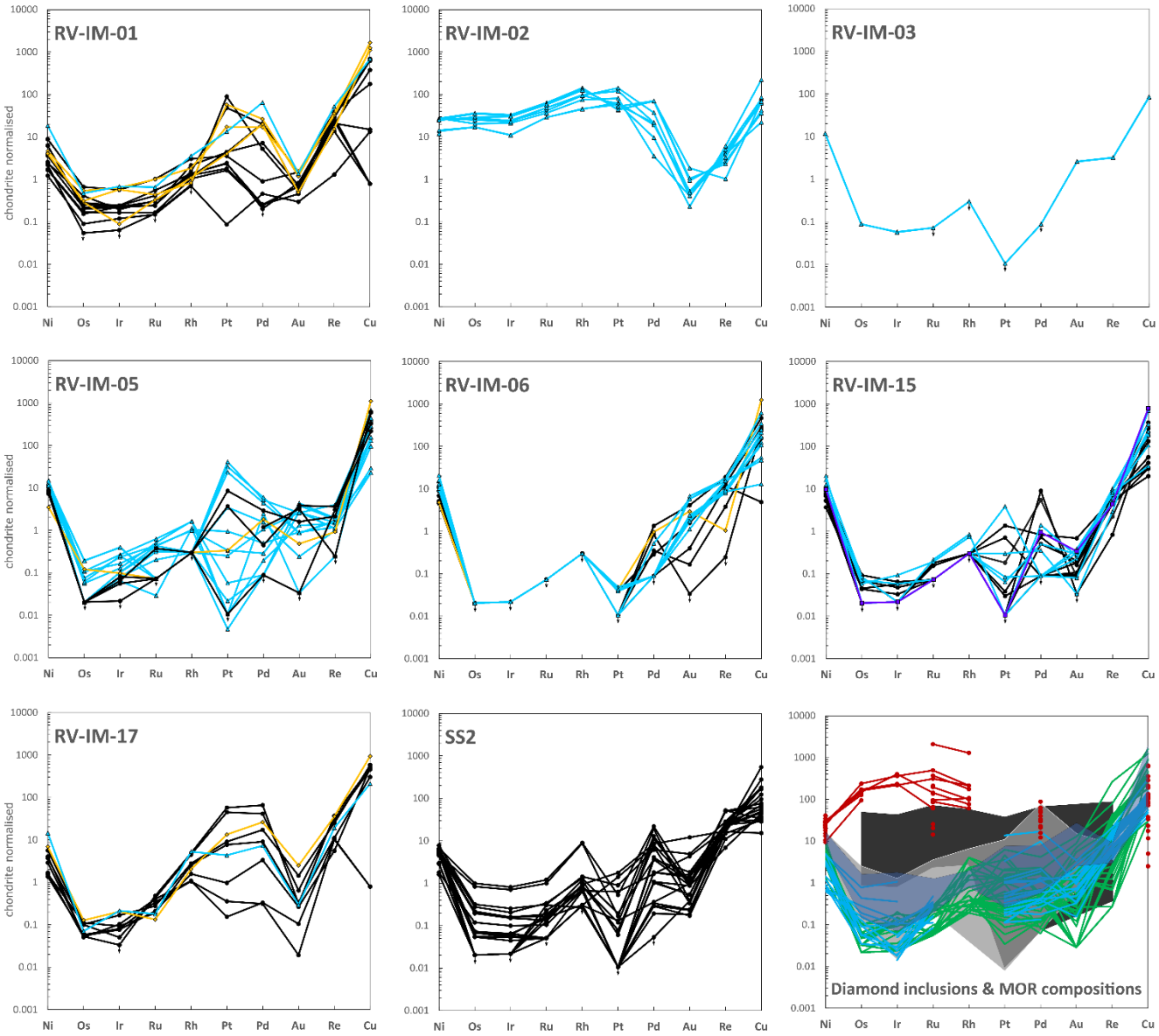
RV-IM-01
RV-IM-02
RV-IM-03
RV-IM-05
RV-IM-06
RV-IM-15
RV-IM-17
SS2
Diamond inclusions & MOR compositions
chondrite normalised
10000
1000
100
10
1
0.1
0.01
0.001
Ni Os Ir Ru Rh Pt Pd Au Re Cu
Roberts Victor eclogite xenolith data (this study):
Fe-(Ni,Cu) BMS
Cu,Fe-(Ni) BMS
Ni,Fe-(Cu) BMS
Ni,Cu,Fe BMS
Diamond inclusion comparison data:
P-type (Bulanova et al., 1996)
E-type (McDonald et al., 2017)
E-type (Aulbach et al., 2012)
Mid-ocean ridge data:
MORB BMS (Patten et al., 2013)
MOR peridotite BMS (Alard et al., 2005)
BMS inclusions in olivine (MOR picrite lavas; Savelyev et al., 2018)

Fig. 7

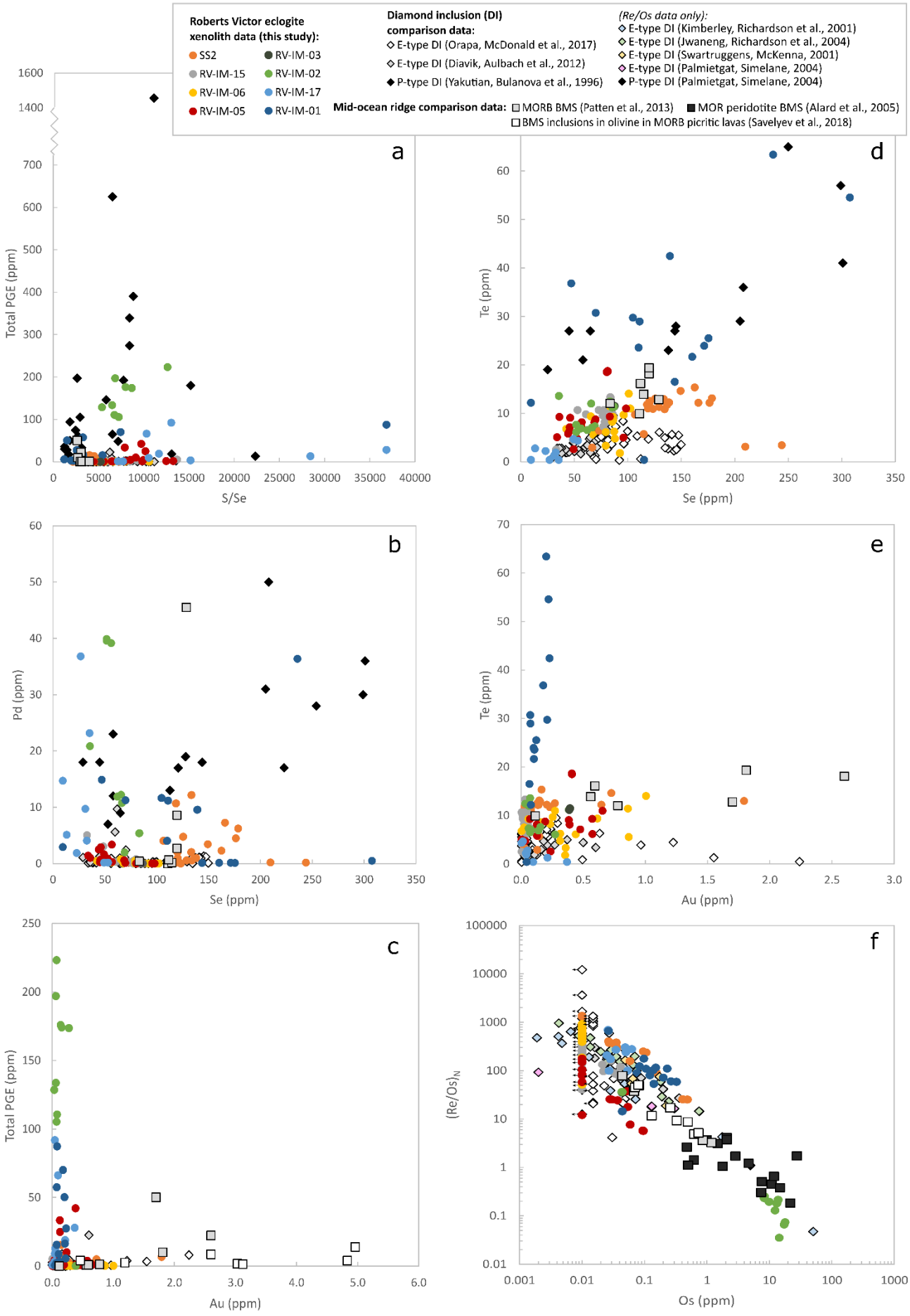
Roberts Victor eclogite xenolith data (this study):
SS2
RV-IM-03
RV-IM-15
RV-IM-02
RV-IM-06
RV-IM-17
RV-IM-05
RV-IM-01
Diamond inclusion (DI) comparison data:
E-type DI (Orapa, McDonald et al., 2017)
E-type DI (Diavik, Aulbach et al., 2012)
P-type DI (Yakutian, Bulanova et al., 1996)
(Re/Os data only):
E-type DI (Kimberley, Richardson et al., 2001)
E-type DI (Jwaneng, Richardson et al., 2004)
E-type DI (Swartruggens, McKenna, 2001)
E-type DI (Palmietgat, Simelane, 2004)
P-type DI (Palmietgat, Simelane, 2004)
Mid-ocean ridge comparison data:
MORB BMS (Patten et al., 2013)
MOR peridotite BMS (Alard et al., 2005)
BMS inclusions in olivine in MORB picritic lavas (Savelyev et al., 2018)
a
Total PGE (ppm)
S/Se
d
Te (ppm)
Se (ppm)
b
Pd (ppm)
Se (ppm)
e
Te (ppm)
Au (ppm)
c
Total PGE (ppm)
Au (ppm)
f
(Re/Os)N
Os (ppm)

Fig. 8

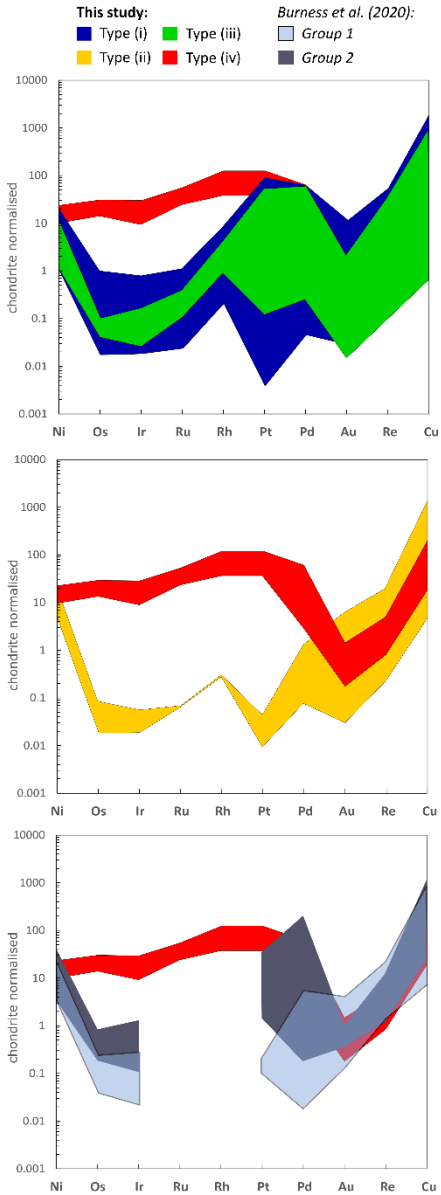
This study:
Type (i)
Type (ii)
Type (iii)
Type (iv)
Burness et al. (2020):
Group 1
Group 2
chondrite normalised
10000
1000
100
10
1
0.1
0.01
0.001
Ni
Os
Ir
Ru
Rh
Pt
Pd
Au
Re
Cu

Fig. 9

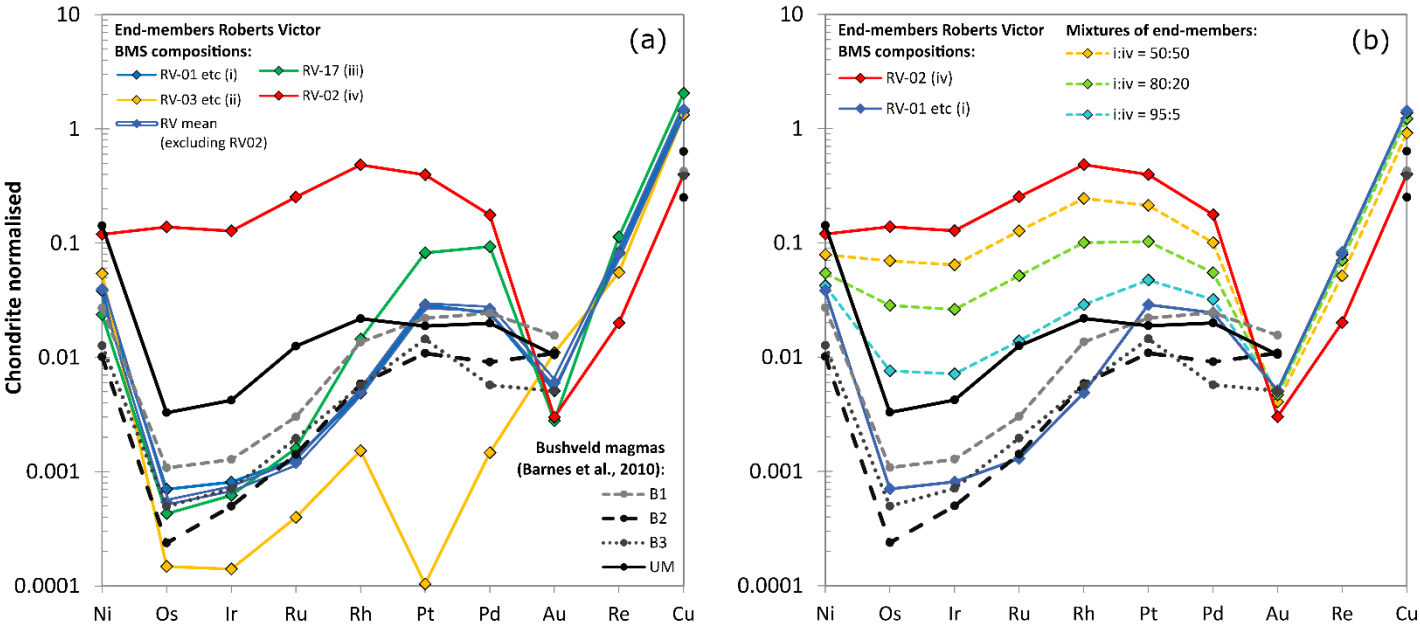
(a)
End-members Roberts Victor
BMS compositions:
RV-01 etc (i)
RV-03 etc (ii)
RV mean
(excluding RV02)
RV-17 (iii)
RV-02 (iv)
Bushveld magmas
(Barnes et al., 2010):
B1
B2
B3
UM
Chondrite normalised
10
1
0.1
0.01
0.001
0.0001
Ni
Os
Ir
Ru
Rh
Pt
Pd
Au
Re
Cu
(b)
End-members Roberts Victor
BMS compositions:
RV-02 (iv)
RV-01 etc (i)
Mixtures of end-members:
i:iv = 50:50
i:iv = 80:20
i:iv = 95:5

Fig. 10

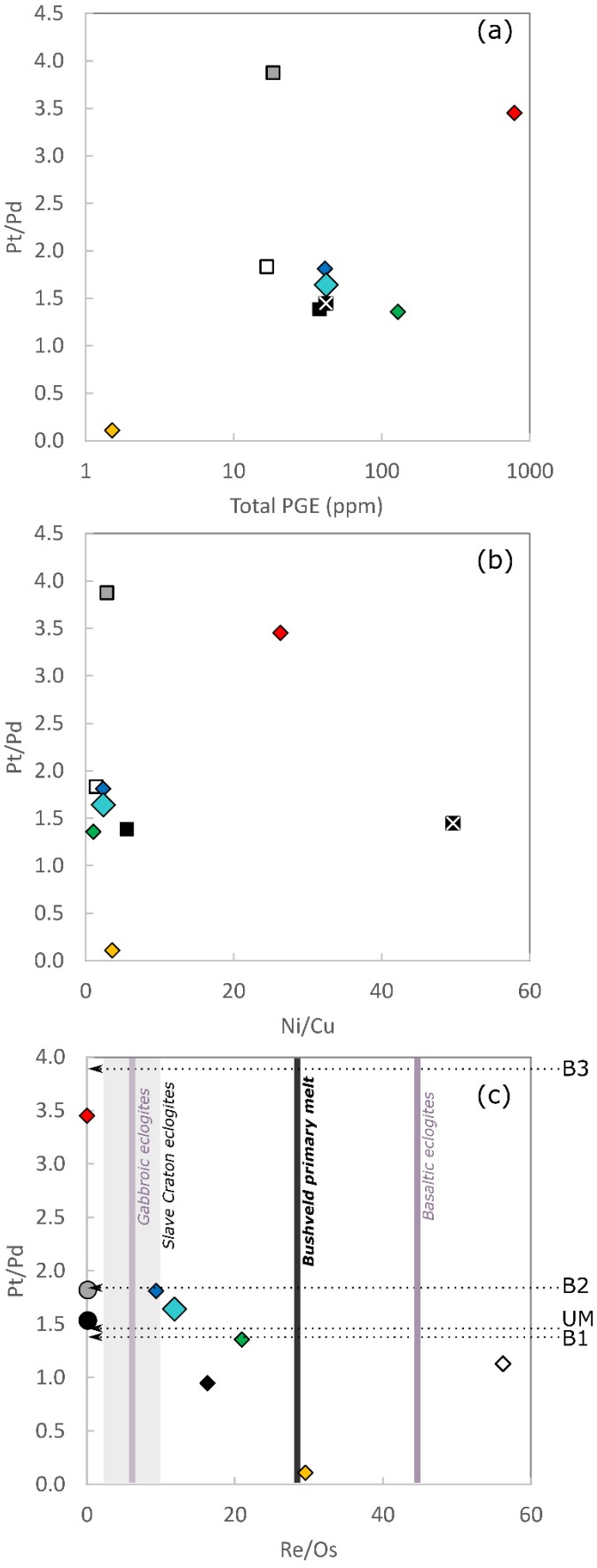
(a)
Pt/Pd
Total PGE (ppm)
(b)
Pt/Pd
Ni/Cu
(c)
Pt/Pd
Re/Os
B3
B2
UM
B1
Gabbroic eclogites
Slave Craton eclogites
Bushveld primary melt
Basaltic eclogites
End-member Roberts Victor BMS compositions:
RV-01 etc (i)
RV-03 etc (ii)
RV-17 (iii)
RV-02 (iv)
RV mean (excluding RV02)
Diamond BMS inclusions (DI):
Diavik E-type DI (Aulbach et al., 2012)
Orapa E-type DI (McDonald et al., 2017))
Bushveld magmas (Barnes et al., 2010):
B1
B2
B3
UM

Table 1

| Sample # | Modal mineralogy | Petrographic siting of BMS |
|---|---|---|
| RV-IM-01 | 60% CPX, 30% Grt, 5% Phl, 5% accessories (including Chl, Tlc, Alb and KFs, Apt and oxides) | Interstitial |
| RV-IM-02 | 50% CPX, 40% Grt, 10% accessories (including Chl, Tlc, Alb and KFs, Apt, Ilm and Rt) | Interstitial |
| RV-IM-03 | - | - |
| RV-IM-05 | 60% CPX, 30% Grt, 10% accessories (including Chl, Tlc, Alb and KFs, Apt, Ilm and Rt) | Interstitial |
| RV-IM-06 | 25% CPX, 70% Grt, 5% (including Chl, Tlc, Alb and KFs, Apt, Ilm and Rt) | Interstitial & Enclosed |
| RV-IM-15 | 50% CPX, 40% Grt, 10% (including Chl, Tlc, Alb and KFs, Apt, Ilm and Rt) | Interstitial & Enclosed |
| RV-IM-17 | - | Interstitial |
| SS2 * | CPX 50%, Grt 50%, accessory Ilm | Interstitial & Enclosed |

Table 2

| % | RV-IM-01 | | RV-IM-15 | | | RV-IM-18 | |
|---|---|---|---|---|---|---|---|
| | * | | | | | | |
| **Pyrite** | 70.6 | 51.6 | 16.1 | 51.2 | 68.5 | 63.0 | 21.7 |
| **Pyrrhotite** | 1.9 | 0.1 | - | 0.1 | 0.6 | 5.0 | - |
| **Chalcopyrite** | 12.4 | 41.3 | 42.4 | 8.5 | 5.7 | 7.4 | 22.1 |
| **Pentlandite** | 15.1 | 7.0 | 41.5 | 40.2 | 25.2 | 24.7 | 56.2 |

Table 3

| Sample | Mineral | *n* | | S | Fe | Ni | Cu | Co | Total | S | Fe | Ni | Cu | Co |
|---|---|---|---|---|---|---|---|---|---|---|---|---|---|---|
| | | | | *(wt%)* | | | | | | *(at%)* | | | | |
| **RV-IM-02** | **Py (± Ni)** | *3* | mean | 53.19 | 44.92 | 0.66 | 0.45 | 0.15 | 99.37 | 66.77 | 32.39 | 0.45 | 0.29 | 0.10 |
| | | | *2 σ* | *0.63* | *0.99* | *0.96* | *1.07* | *0.17* | *0.62* | *0.67* | *0.73* | *0.66* | *0.68* | *0.11* |
| **RV-IM-06** | **Po** | *3* | mean | 40.14 | 56.77 | 2.43 | < LLD | 0.11 | 99.46 | 54.15 | 43.98 | 1.79 | < LLD | 0.08 |
| | | | *2 σ* | *1.59* | *3.44* | *1.42* | - | *0.13* | *0.51* | *1.88* | *2.86* | *1.04* | - | *0.10* |
| **RV-IM-15** | **Cp** | *2* | mean | 35.29 | 30.17 | 0.24 | 33.75 | 0.08 | 99.53 | 50.54 | 24.82 | 0.19 | 24.39 | 0.06 |
| | | | *2 σ* | *0.11* | *0.11* | *0.25* | *0.25* | *0.01* | *0.71* | *0.15* | *0.06* | *0.19* | *0.03* | *0.01* |
| | **Py (± Ni)** | *6* | mean | 52.91 | 45.66 | 0.71 | 0.12 | 0.13 | 99.52 | 66.42 | 32.92 | 0.49 | 0.07 | 0.09 |
| | | | *2 σ* | *1.06* | *1.56* | *1.18* | *0.21* | *0.14* | *1.00* | *0.63* | *0.99* | *0.81* | *0.13* | *0.10* |
| **RV-IM-18** | **Py (± Ni)** | *1* | - | 52.09 | 43.78 | 3.00 | 0.08 | 0.20 | 99.15 | 65.92 | 31.82 | 2.07 | 0.05 | 0.14 |
| **SS2** | **Cp** | *10* | mean | 35.40 | 30.24 | 0.14 | 33.52 | 0.08 | 99.36 | 50.72 | 24.89 | 0.11 | 24.24 | 0.06 |
| | | | *2 σ* | *1.11* | *0.74* | *0.17* | *0.69* | *0.09* | *0.64* | *1.07* | *0.74* | *0.14* | *0.66* | *0.07* |
| | **Py (± Ni)** | *21* | mean | 53.20 | 43.93 | 2.20 | 0.26 | 0.30 | 99.86 | 66.58 | 31.57 | 1.51 | 0.17 | 0.21 |
| | | | *2 σ* | *0.88* | *3.29* | *3.42* | *0.56* | *0.33* | *1.02* | *0.46* | *2.30* | *2.35* | *0.35* | *0.22* |

Table 5

| Sample | *n* | Interstitial (%) | Included (%) |
|---|---|---|---|
| RV-IM-02 | *2* | 100 | - |
| RV-IM-03 | *2* | 100 | - |
| RV-IM-05 | *4* | 100 | - |
| RV-IM-06 | *9* | 11 | 89 |
| RV-IM-15 | *8* | 75 | 25 |
| SS2 | *53* | 89 | 11 |
| Total | *78* | 79 | 21 |

Table 4

| Sample | Analysis # | *n* | | 33S (wt%) | S/Se | Fe (wt%) | Co (ppm) | Ni (wt%) | Cu | Zn (ppm) | As | Se | Ru | Rh | Pd | Ag | Cd | Sb | Te | Re | Os | Ir | Pt | Au | Bi |
|---|---|---|---|---|---|---|---|---|---|---|---|---|---|---|---|---|---|---|---|---|---|---|---|---|---|
| **SS2** | All (Py ± Ni) | *23* | mean | 53.5 | 4185 | 39.21 | 2840 | 5.42 | 1.25 | 17 | 198 | 138 | 0.15 | 0.18 | 2.83 | 3.48 | 1.32 | 3.54 | 10.51 | 1.00 | 0.08 | 0.06 | 0.25 | 0.24 | 0.21 |
| | | | *σ* | - | *1302* | *1.92* | *616* | *1.68* | *1.48* | *16* | *201* | *39* | *0.20* | *0.32* | *3.43* | *6.27* | *1.92* | *3.28* | *3.61* | *0.47* | *0.12* | *0.10* | *0.45* | *0.38* | *0.10* |
| **RV15** | Pn and Ni-rich BMS (> 10 wt.% Ni) | *8* | mean | 45 | 6105 | 35.69 | 5125 | 13.53 | 4.14 | 365 | 406 | 76 | 0.07 | 0.06 | 0.25 | 8.13 | 4.7 | 9.16 | 9.75 | 0.27 | 0.02 | 0.02 | 0.51 | 0.04 | 0.36 |
| | | | *σ* | - | *1186* | *4.62* | *1554* | *3.91* | *3.47* | *257* | *334* | *12* | *0.04* | *0.03* | *0.28* | *4.09* | *2.7* | *4.56* | *2.08* | *0.10* | *0.01* | *0.01* | *1.26* | *0.02* | *0.18* |
| | Fe-rich BMS ± Ni (< 10 wt.% Ni) | *9* | mean | 45 | 6959 | 44.61 | 3413 | 7.48 | 1.58 | 117 | 1634 | 71 | 0.06 | 0.04 | 1.05 | 5.42 | 1.4 | 13.80 | 7.86 | 0.20 | 0.02 | 0.02 | 0.25 | 0.03 | 0.16 |
| | | | *σ* | - | *2797* | *2.78* | *1033* | *2.11* | *1.56* | *101* | *630* | *18* | *0.03* | *0.00* | *1.78* | *1.71* | *0.6* | *4.05* | *2.68* | *0.09* | *0.01* | *0.01* | *0.44* | *0.03* | *0.11* |
| **RV06** | Cp | *1* | mean | 45 | 5658 | 31.77 | 2823 | 5.08 | 15.80 | 174 | 8 | 80 | *0.05* | *0.04* | 0.54 | 3.15 | 8.0 | 9.68 | 6.10 | 0.04 | *0.01* | *0.01* | 0.04 | 0.44 | 0.24 |
| | | | | - | - | - | - | - | - | - | - | - | - | - | - | - | - | - | - | - | - | - | - | - | - |
| | Pn and Ni-rich BMS (> 10 wt.% Ni) | *10* | mean | 45 | 5154 | 37.18 | 5406 | 14.16 | 2.46 | 39 | 17 | 88 | 0.05 | 0.04 | 0.07 | 4.31 | 1.0 | 11.07 | 7.64 | 0.51 | 0.01 | 0.01 | 0.02 | 0.48 | 0.81 |
| | | | *σ* | - | *656* | *3.97* | *2090* | *3.50* | *2.30* | *33* | *9* | *10* | *0.00* | *0.00* | *0.08* | *1.51* | *0.5* | *5.75* | *3.92* | *0.16* | *0.00* | *0.00* | *0.01* | *0.31* | *0.71* |
| | Fe-rich BMS ± Ni (< 10 wt.% Ni) | *5* | mean | 45 | 7181 | 44.34 | 2335 | 6.49 | 2.94 | 50 | 6 | 67 | 0.05 | 0.04 | 0.33 | 1.62 | 1.1 | 4.71 | 8.23 | 0.38 | 0.01 | 0.01 | 0.02 | 0.19 | 0.65 |
| | | | *σ* | - | *2232* | *4.11* | *861* | *1.88* | *2.15* | *35* | *9* | *19* | *0.00* | *0.00* | *0.29* | *1.10* | *0.4* | *3.87* | *1.11* | *0.30* | *0.00* | *0.00* | *0.01* | *0.26* | *0.43* |
| **RV05** | Cp | *1* | mean | 45 | 12492 | 36.45 | 2173 | 3.72 | 14.13 | 204 | 20 | 36 | *0.05* | *0.04* | 1.03 | 0.66 | 3.6 | 16.93 | 9.26 | 0.04 | 0.06 | 0.05 | 0.32 | 0.07 | 0.19 |
| | | | | - | - | - | - | - | - | - | - | - | - | - | - | - | - | - | - | - | - | - | - | - | - |
| | Pn and Ni-rich BMS (> 10 wt.% Ni) | *12* | mean | 45 | 7635 | 37.24 | 5334 | 12.97 | 3.07 | 115 | 1197 | 64 | 0.20 | 0.09 | 1.03 | 4.73 | 2.0 | 110.54 | 9.51 | 0.06 | 0.04 | 0.09 | 7.96 | 0.29 | 0.72 |
| | | | *σ* | - | *2507* | *2.73* | *820* | *1.71* | *2.59* | *46* | *632* | *19* | *0.14* | *0.07* | *1.23* | *2.15* | *1.7* | *34.13* | *4.61* | *0.04* | *0.03* | *0.06* | *13.92* | *0.21* | *0.74* |
| | Fe-rich BMS ± Ni (< 10 wt.% Ni) | *4* | mean | 45 | 8399 | 40.36 | 3420 | 8.34 | 5.56 | 200 | 4646 | 59 | 0.10 | 0.04 | 0.65 | 5.22 | 2.0 | 127.05 | 5.22 | 0.09 | 0.01 | 0.03 | 2.88 | 0.32 | 0.22 |
| | | | *σ* | - | *2504* | *4.61* | *621* | *0.80* | *2.49* | *71* | *4492* | *25* | *0.10* | *0.00* | *0.71* | *2.83* | *1.4* | *37.16* | *1.96* | *0.06* | *0.00* | *0.01* | *3.81* | *0.25* | *0.08* |
| **RV02** | Pn and Ni-rich BMS (> 10 wt.% Ni) | *9* | mean | 45 | 7864 | 27.43 | 16446 | 25.10 | 0.95 | 98 | 114 | 60 | 31.81 | 12.69 | 20.20 | 12.69 | 2.4 | 44.81 | 8.84 | 0.15 | 12.85 | 10.76 | 69.72 | 0.11 | 1.34 |
| | | | *σ* | - | *2084* | *5.08* | *7429* | *5.87* | *0.75* | *44* | *119* | *13* | *9.14* | *4.80* | *15.39* | *3.44* | *1.4* | *13.03* | *2.94* | *0.06* | *3.48* | *3.76* | *32.85* | *0.07* | *0.57* |
| **RV03** | Pn and Ni-rich BMS (> 10 wt.% Ni) | *2* | mean | 45 | 5206 | 39.15 | 3851 | 12.59 | 1.08 | 61 | 451 | 86 | 0.05 | 0.04 | 0.05 | 10.34 | 2.4 | 14.46 | 11.25 | 0.13 | 0.04 | 0.03 | 0.01 | 0.39 | 0.25 |
| | | | *σ* | - | *71* | *0.48* | *45* | *0.13* | *0.02* | *2* | *5* | *1* | *0.00* | *0.00* | *0.00* | *0.11* | *0.1* | *0.14* | *0.13* | *0.00* | *0.00* | *0.00* | *0.00* | *0.00* | *0.00* |
| **RV17** | Cp | *1* | - | 38 | 36842 | 44 | 4855 | 7.34 | 11.92 | 226 | 143 | 10 | 0.09 | 0.27 | 14.72 | 58.99 | 11.38 | 6.84 | *0.40* | 1.45 | 0.06 | 0.09 | 12.64 | 0.37 | 0.25 |
| | | | | - | - | - | - | - | - | - | - | - | - | - | - | - | - | - | - | - | - | - | - | - | - |
| | Pn and Ni-rich BMS (> 10 wt.% Ni) | *1* | - | 36.5 | 10567 | 46 | 12263 | 15.31 | 2.68 | 76 | 563 | 33 | 0.12 | 0.70 | 4.09 | 167.52 | 3.86 | 26.18 | 1.90 | 0.78 | 0.03 | 0.10 | 4.10 | 0.04 | 0.04 |
| | | | | - | - | - | - | - | - | - | - | - | - | - | - | - | - | - | - | - | - | - | - | - | - |
| | Fe-rich BMS ± Ni (< 10 wt.% Ni) | *7* | mean | 36 | 13362 | 56 | 2792 | 3.17 | 4.24 | 58 | 1040 | 33 | 0.23 | 0.35 | 11.01 | 111.23 | 2.50 | 14.75 | 2.30 | 0.75 | 0.04 | 0.04 | 16.18 | 0.07 | 0.26 |
| | | | *σ* | - | *7228* | *3* | *1209* | *1.69* | *3.08* | *48* | *598* | *14* | *0.08* | *0.21* | *13.96* | *105.35* | *2.62* | *4.92* | *1.75* | *0.49* | *0.01* | *0.02* | *22.29* | *0.07* | *0.31* |
| **RV01** | Cp | *3* | mean | 36.5 | 5164 | 42 | 2309 | 4.53 | 16.95 | 637 | 181 | 85 | 0.40 | 0.17 | 11.90 | 38.62 | 2.14 | 36.44 | 36.66 | 1.14 | 0.19 | 0.20 | 24.87 | 0.16 | 0.18 |
| | | | *σ* | - | *2422* | *3* | *382* | *0.35* | *3.79* | *231* | *74* | *48* | *0.25* | *0.07* | *2.72* | *26.37* | *1.04* | *13.14* | *5.86* | *0.45* | *0.07* | *0.14* | *26.40* | *0.08* | *0.13* |
| | Pn and Ni-rich BMS (> 10 wt.% Ni) | *1* | - | 36 | 1527 | 36 | 6351 | 19.51 | 8.70 | 670 | 119 | 236 | 0.45 | 0.47 | 36.37 | 130.13 | 0.74 | 73.60 | 63.39 | 2.11 | 0.23 | 0.31 | 12.46 | 0.20 | 0.26 |
| | | | | - | | - | - | - | - | - | - | - | - | - | - | - | - | - | - | - | - | - | - | - | - |
| | Fe-rich BMS ± Ni (< 10 wt.% Ni) | *9* | mean | 36 | 6439 | 52 | 1911 | 3.78 | 3.56 | 3189 | 942 | 139 | 0.25 | 0.19 | 3.44 | 26.41 | 2.01 | 37.90 | 23.92 | 0.99 | 0.11 | 0.11 | 16.40 | 0.11 | 0.12 |
| | | | *σ* | - | *11424* | *9* | *1882* | *2.67* | *3.81* | *7426* | *1615* | *80* | *0.19* | *0.10* | *4.74* | *31.78* | *3.86* | *21.26* | *14.78* | *0.49* | *0.09* | *0.06* | *29.18* | *0.06* | *0.06* |

## Chalcophile and PGE modelling:

In order to evaluate the PGE budget of the eclogitic SCLM, we calculated the bulk concentration of Ni, Cu, Au, Re and the PGE in a silicate magma produced by partial melting of BMS as represented by Roberts Victor eclogite xenolith and compared this to the bulk rock compositions of parental Bushveld magmas (B1, B2 and B3, after Barnes et al., 2010). This method was chosen for two reasons: (i) eclogite xenoliths are small and thus bulk rock analyses are rare or inappropriate and (ii) chalcophile elements, such as the PGE, are primarily controlled by sulphide minerals during partial melting and fractionation, hence the sulphide composition for PGE is of most relevance when considering mantle reservoir compositions and budgets available during partial melting.

We use a batch partial melting model (after Shaw, 2006) from of:

$$\frac{C_L}{C_0} = {}^{1}/_{D + F(1 - D)}$$

where $C_L$ = concentration in liquid, $C_0$ = initial concentration, $F$ = fraction of melting, and $D$ = bulk distribution coefficient.

This assumes that the eclogite is primarily composed of clinopyroxene and garnet (in equal proportions) and 0.5 volume % BMS (total). This proportion of BMS is based on our observations of the abundance of BMS in Roberts Victor eclogite xenoliths (see main text for further information). For the purposes of this modelling, we do not distinguish between MSS, ISS or any end-member sulphide mineral but instead assume a total BMS composition and model the partial melting of this whole BMS. Partition coefficients of all chalcophile elements were set to $10^{-7}$ in clinopyroxene and garnet (i.e., highly incompatible). Partition coefficients for chalcophile elements in BMS were as follows (from Mungall and Brenan, 2014): 500 (Ni), 3 x $10^5$ (Os), 1.9 x $10^6$ (Ir), 4.85 x $10^5$ (Ru), 5.91 x $10^5$ (Rh), 3.45 x $10^6$ (Pt), 5.36 x $10^5$ (Pd), 6307 (Au), 800 (Re), 1472 (Cu).

By multiplying the abundance of each mineral by the partition coefficient of each element, a bulk distribution coefficient ($D$) for each element for the bulk rock was calculated. This $D$ value was then applied to the batch partial melting equation (above). A range of degrees of partial melting ($F$) were used to calculate the composition of the liquid ($C_L$) formed through partial melting. The composition of BMS used in models were also varied (ranging the four 'types' of BMS identified in Roberts Victor xenoliths from this study – table below and see main text for more details). These $C_L$ compositions were then used in compositional plots (e.g., Figs. 9 and 10). As these represent bulk liquid compositions, no recalculation of B1, B2 or B3 is necessary. Multi-element diagrams show concentrations normalized to chondrite (normalization values from Fischer-Gödde et al., 2010).

Table of starting compositions (BMS end-members) used in modelling

| | **Ni** *(wt.%)* | **Os** *(ppm)* | **Ir** | **Ru** | **Rh** | **Pt** | **Pd** | **Au** | **Re** | **Cu** *(wt.%)* |
|---|---|---|---|---|---|---|---|---|---|---|
| **Type i** | 8.00 | 0.07 | 0.07 | 0.16 | 0.13 | 5.06 | 2.79 | 0.18 | 0.61 | 3.44 |
| **Type ii** | 11.35 | 0.01 | 0.01 | 0.05 | 0.04 | 0.02 | 0.17 | 0.38 | 0.41 | 3.18 |
| **Type iii** | 4.98 | 0.04 | 0.05 | 0.20 | 0.38 | 14.44 | 10.65 | 0.10 | 0.83 | 4.92 |
| **Type iv** | 25.10 | 12.85 | 10.76 | 31.81 | 12.69 | 69.72 | 20.20 | 0.11 | 0.15 | 0.95 |
| **RV mean (excluding RV-IM-02, Type iv)** | 8.34 | 0.05 | 0.06 | 0.15 | 0.13 | 4.99 | 3.04 | 0.21 | 0.59 | 3.53 |